tektonika

Setting the Sequence of Slicing Events Along Deep Subduction Interfaces:

2. P-T Conditions and Timing of Accretion and Exhumation in Western Crete (Hellenic Margin)

Armel Menant *[1,2], **Johannes Glodny** [2], **Samuel Angiboust** [3,4], **Edward R. Sobel** [5],
Eloïse Bessière [1], **Laurent Jolivet** [6], **Romain Augier** [7], **Onno Oncken** [2]

[1]Université Côte d'Azur, CNRS, Observatoire de la Côte d'Azur, IRD, Géoazur, Valbonne, France | [2]GFZ Helmholtz Centre Potsdam, German Research Centre for Geosciences, Potsdam, Germany | [3]École Normale Supérieure of Lyon, Université de Lyon, LGL-TPE, Lyon, France | [4]Institut Universitaire de France (IUF), Paris, France | [5]Institute of Geosciences, Universität Potsdam, Potsdam-Golm, Germany | [6]Sorbonne Université, CNRS-INSU, Institut des Sciences de la Terre de Paris (ISTeP), UMR7193, Paris, France | [7]Université d'Orléans, CNRS, BRGM, Institut de Sciences de la Terre d'Orléans (ISTO), UMR7327, Orléans, France

Abstract To understand basal-accretion dynamics in subduction zones and forearc crustal response, it is crucial to constrain the timing of slicing events forming high pressure-low temperature accretionary duplexes. This, the second of two companion papers in this issue of Tektonika, investigates the pressure-temperature-time history of tectono-metamorphic units in the paleo-duplex of western Crete, accreted along the Hellenic subduction zone during the late Oligocene-Miocene. Petrological characterization, thermodynamic modeling and a data review reveal peak metamorphic conditions evolving from 17-18 kbar and 410-430 °C to 7-8.5 kbar and 310-360 °C from top to base of the nappe stack. These results suggest a decrease in basal-accretion depth from 55-60 km to 25-30 km, likely linked to an increase in the subduction-related geothermal gradient. New Rb/Sr multi-mineral ages show a consistent decrease toward the base of the duplex, except for the lowermost Plattenkalk Unit. These ages, along with the down-stepping of peak conditions, reveal two slicing episodes between ~26 Ma and ~15 Ma, and likely three additional events from the late Oligocene to middle Miocene. (U-Th-Sm)/He thermochronology on zircon indicates rapid exhumation during the middle Miocene, with rates of ~3-11 mm/yr, decreasing to ~2-4 mm/yr at shallow levels. These successive accretion-then-exhumation episodes were driven by the accelerating southward retreat of the Hellenic subduction, enhanced by slab tearing from ~15 Ma, contributing to the geothermal gradient increase. This study further suggests a sequence of ~2-3-Myr-long deep slicing events, providing a critical timescale for monitoring the tectonic and topographic signatures of deep mass fluxes along active margins worldwide. It also supports ongoing basal-accretion events beneath Crete, contributing to the island's emergence.

Executive Editor:
Graeme Eagles
Associate Editor:
Adrian Castro
Technical Editor:
Mohamed Gouiza

Reviewers:
Reviewer 1 (Anonymous)
Reviewer 2 (Anonymous)

Submitted:
31 March 2025
Accepted:
27 February 2025
Published:
9 April 2026

1 Introduction

Geometry and deformation monitored along active forearc margins are significantly controlled by tectonic mass transfers that occur at >20-km depth along subduction interfaces (*von Huene and Scholl*, 1991; *Gutscher et al.*, 1996; *Clift and Vannucchi*, 2004; *Noda*, 2016; *Menant et al.*, 2020). Key insights on the dynamics of these deep processes, and notably on basal-accretion events suspected along many active subduction zones worldwide (*Scholl*, 2021), can be obtained by studying the pressure-temperature-time (P-T-t) history of now-exhumed accretionary duplexes in which each coherent tectono-metamorphic unit witnesses a distinct slicing event. Such investigations may shed light on the spatial extent and the recurrence time of these mass fluxes and therefore on their tectonic and topographic signature in the overriding forearc crust.

In two companion papers published together in this Tektonika issue, we report a multi-disciplinary study to unravel the tectono-metamorphic evolution of the paleo-accretionary duplex exposed in western Crete (Greece; Figure 1) (*Creutzburg and Seidel*, 1975; *Seidel et al.*, 1982; *Fassoulas et al.*, 1994; *Jolivet et al.*, 1994, 1996; *Papanikolaou and Vassilakis*, 2010). In the first contribution (*Menant et al.*, 2026, this issue), we discussed the 3D crustal-scale geometry and thermal architecture of the high pressure-low temperature (HP-LT) metamorphic stack based on new field observations, structural analysis

---

*✉ armel.menant@geoazur.unice.fr

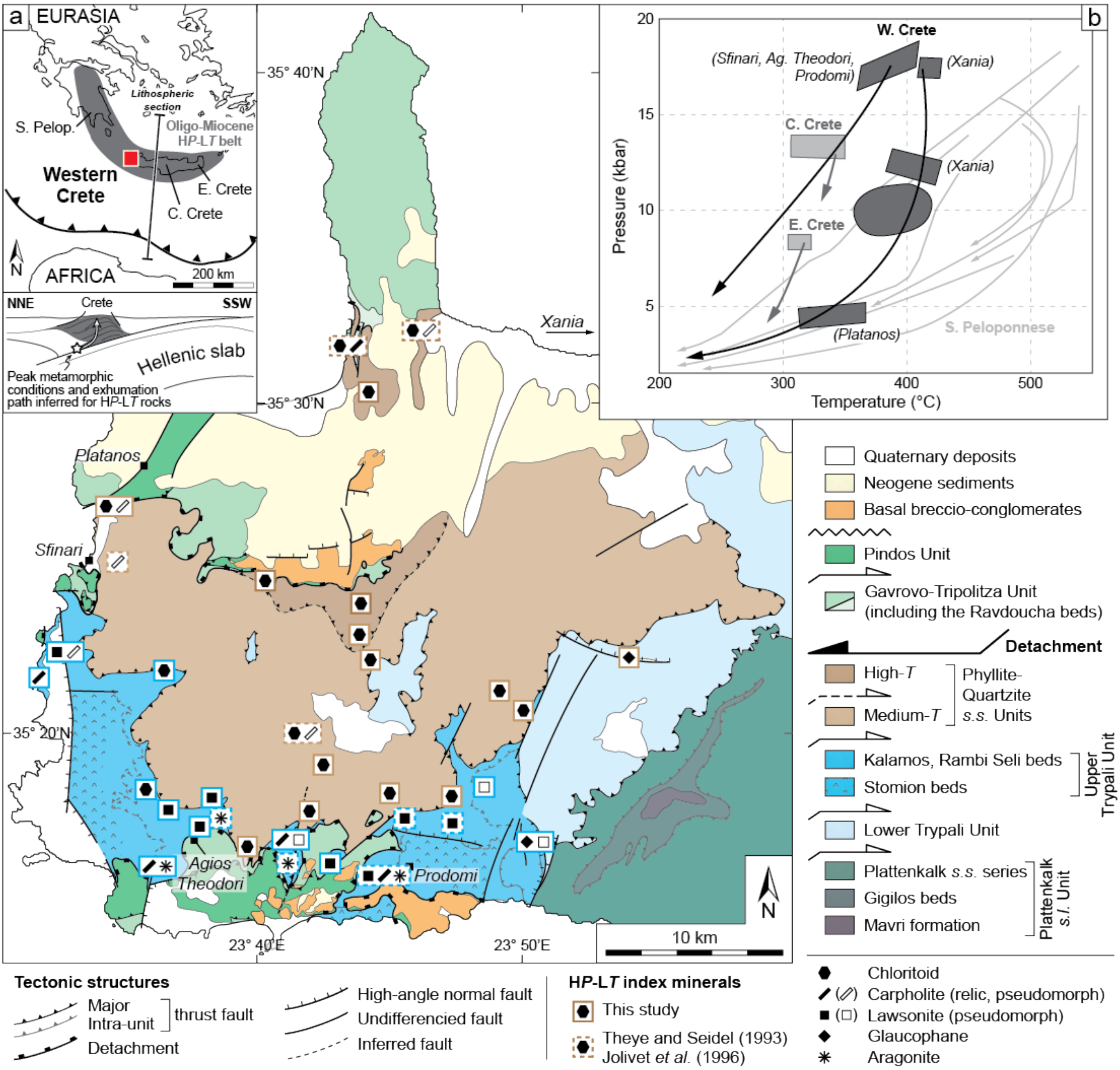

Figure 1 – (**a**) Geological and petrological map of western Crete compiled from *Creutzburg and Seidel* (1975), *Chatzaras et al.* (2013), *Zulauf et al.* (2018) and this study. Location of H*P*-L*T* index minerals is based on macroscopic and microscopic observations. (**b**) Compilation of *P-T* paths for the Phyllite-Quartzite *s.l.* Unit in Crete and south Peloponnese (*Vidal et al.*, 1992; *Jolivet et al.*, 1996, 2010; *Bouhot et al.*, 2025).

and Raman spectrometry on carbonaceous material (RSCM) geothermometry. Five tectono-metamorphic units bounded by major shear zones and characterized by a distinct thermal signature have thus been identified. The units form a dome-like structure topped by several low-angle normal fault zones (i.e., the detachments), with a dominant top-to-the-north kinematics, that accommodated a N-S-directed bivergent extension later evolving in an E-W-directed trench-parallel extension.

This second contribution provides new petrological observations, thermodynamic modeling results, Rb/Sr multi-mineral geochronology and (U-Th-Sm)/He thermochronology on zircon in order to reconstruct the journeys of several metamorphic units from the subduction interface to the shallow forearc crust. Distinct ages for the H*P*-L*T* peak metamorphic event and the subsequent retrogression stage for several accreted units show that slicing episodes along the Hellenic subduction zone were separated by a few Myr during the late Oligocene to middle Miocene, before the whole nappe stack was rapidly exhumed to the surface. These results (i) demonstrate the high rate of syn-orogenic exhumation during fast slab roll-back and (ii) provide important time constraints regarding the recurrence interval of basal-accretion events and the associated tectonic and topographic signals that can be monitored at active margins worldwide.

2 Geological Setting

The nappe stack of western Crete is part of the forearc domain of the active Hellenic subduction zone, driven by the convergence between Africa and Eurasia since the Mesozoic (*Menant et al.*, 2016a; *van Hinsbergen et al.*, 2020). It forms part of the Oligocene-Miocene HP-LT belt that extends from Crete to Peloponnese, resulting from the accretion of two primary tectono-metamorphic assemblages (i.e., the Phyllite-Quartzite *sensu lato* (*s.l.*) Unit and the Plattenkalk *s.l.* Unit) that contributed to the growth of the Hellenides. Simultaneously, the southward retreat of the Hellenic slab triggered the opening of the Aegean back-arc domain further north (*Papanikolaou*, 1997; *Jolivet and Brun*, 2010).

This section synthesizes existing petrological observations, P-T estimates and geochronological and thermochronological constraints for the Phyllite-Quartzite *s.l.* Unit and the Plattenkalk *s.l.* Unit in Crete and the Peloponnese. A more detailed description of the stratigraphy, structure and tectonic contacts observed in the study area is provided in Section 2 of the companion paper (*Menant et al.*, 2026, this issue).

2.1 Metamorphic Record of the Hellenic Subduction in Crete-Peloponnese

The lowermost Plattenkalk *s.l.* Unit (also known as the Mani Unit; *Papanikolaou and Vassilakis*, 2010) generally lacks index minerals for HP-LT metamorphism due to the dominance of carbonates, although Fe-Mg-carpholite, along with coexisting pyrophyllite and diaspore, has been identified in central Crete and southern Peloponnese, suggesting P-T conditions of 7-8.5 kbar and 310-360 °C (*Seidel et al.*, 1982; *Blumör et al.*, 1994). Overlying this unit, the Phyllite-Quartzite *s.l.* Unit commonly shows blueschist-facies metamorphism with varying HP-LT parageneses. In eastern Crete, Fe-Mg-carpholite, pyrophyllite and chlorite indicate peak metamorphic conditions of ~8 kbar and ~300 °C (Figure 1b) (*Seidel et al.*, 1982; *Theye et al.*, 1992). In central Crete, chloritoid appears at the expense of Fe-Mg-carpholite and is associated with moderately substituted phengite (Si^{4+} content of 3.1 atoms per formula unit: apfu), suggesting conditions of 9-12 kbar and 330-350 °C (*Theye et al.*, 1992; *Jolivet et al.*, 1996). A similar reaction is reported in western Crete but with a higher Mg content for carpholite and chloritoid that indicates conditions of ~10 kbar and ~400 °C (*Theye et al.*, 1992). A higher P estimate of 16 ± 2 kbar has also been proposed in this region, based on the recognition of phengite with higher Si^{4+} content (3.3-3.4 apfu) (*Jolivet et al.*, 1996). In this area, glaucophane has also been locally observed in metavolcanics (*Seidel et al.*, 1982). In southwestern Crete, lawsonite-bearing aragonite marbles and metapelites, along with well-preserved carpholite-bearing tensile veins, have been reported (*Seidel*, 1978; *Theye and Seidel*, 1993), suggesting rapid cooling during the retrogression stage (Figure 1b (*Jolivet et al.*, 1996). In Peloponnese, the Phyllite-Quartzite *s.l.* Unit is made up of by four tectono-metamorphic units characterized by HP-LT parageneses with glaucophane, chloritoid, pyrophyllite, Fe-Mg-carpholite and locally garnet with peak conditions ranging from 12-18 kbar and 450-550 °C (*Seidel et al.*, 1982; *Theye et al.*, 1992; *Trotet et al.*, 2006; *Jolivet et al.*, 2010; *Bouhot et al.*, 2025). On the neighboring island of Kythira, garnet, chloritoid and glaucophane are reported in both the Phyllite-Quartzite *s.l.* Unit and the pre-Alpine basement that experienced conditions of 370-450 °C and 7-9 kbar and 5-7 kbar, respectively (*Romer et al.*, 2008). Excluding the latter, these P-T records highlight a trench-parallel variation of the metamorphic conditions, from a cooler regime in eastern Crete to a warmer one toward the Peloponnese (Figure 1b; *Jolivet et al.*, 2010).

2.2 Age Constraints on Subduction-related Metamorphism and Cooling

In Crete and Peloponnese, the timing of the HP-LT metamorphism in the Phyllite-Quartzite *s.l.* Unit has been constrained by K/Ar and $^{40}Ar/^{39}Ar$ dating on white mica, yielding ages of ~20-25 Ma for western Crete (*Seidel et al.*, 1982; *Jolivet et al.*, 1996) and 13-26 Ma for southern Peloponnese and Kythira (*Seidel et al.*, 2006; *Jolivet et al.*, 2010). However, U/Pb dating of aragonite-bearing veins suggest younger ages of ~13-16 Ma in western Crete (*Ring et al.*, 2022), questioning the timing of the HP-LT metamorphism. K/Ar ages on illite/white mica from fault gouges in the same area yielded widespread ages mostly ranging from late Eocene to late Miocene and tentatively interpreted as repeating fault activation during the underthrusting and exhumation (*Ring et al.*, 2022). In eastern Crete, K/Ar dating on riebeckite and whole rock yielded maximum ages of ~57 Ma and 24 Ma, respectively (*Seidel et al.*, 1982), while $^{40}Ar/^{39}Ar$ dating on white mica gave ages ranging from 29-180 Ma (Jolivet *et al.*, 1996) and 91-278 Ma (*Grasemann et al.*, 2019) that are interpreted as a partial resetting of pre-Alpine micas due to low-temperature subduction conditions.

Subsequent cooling of the Phyllite-Quartzite *s.l.* Unit is constrained by zircon fission-track dating in western and central Crete that provided ages ranging between 16.8 ± 1.3 Ma and 22.3 ± 1.3 Ma (*Thomson et al.*, 1998), while *Marsellos et al.* (2010) reported younger ages of ~13.4-17.6. Apatite fission-track ages were also obtained in the same area, ranging from 11.5 ± 2.7 Ma to 18.4 ± 4.1 Ma (*Thomson et al.*, 1998; *Marsellos et al.*, 2010), 2010). In eastern Crete, fission-track ages range from 145 ± 10 Ma to 414 ± 24 Ma, indicating a significant component of inheritance (*Brix et al.*, 2002), while partially reset (U-Th)/He zircon ages range from 12 to 132 Ma, with a weighted mean age of 14.5 ± 0.8 Ma reflecting late exhumation during the activity of the Cretan detachment (*Grasemann et al.*, 2019). Zircon fission-track ages in central-south Peloponnese (~12.8-21.4 Ma) are similar to those from western Crete, but older than those from the southernmost Peloponnese and Kythira (~9.1-12.8 Ma) (*Marsellos et al.*, 2010). In the same region, apatite fission-track dating yielded ages from 6.5±1.1 Ma to 9.8±1.3 Ma (*Marsellos et al.*, 2010).

In summary, the HP-LT event recorded in the Phyllite-Quartzite *s.l.* Unit occurred during the late Oligocene to early Miocene. The subsequent exhumation proceeded at rates 4 mm/yr and was diachronous, starting in Crete and south-central Peloponnese during the middle Miocene, followed by the southernmost Peloponnese and Kythira during the late Miocene.

3 Methods

To characterize the P-T history and the timing of peak metamorphism and subsequent exhumation of the paleo-accretionary complex of western Crete, 18 samples of representative lithotypes were collected from four previously identified tectono-metamorphic units (*Menant et al.*, 2026, this issue), ranging from the top to the base of the nappe stack: the High-T and Medium-T Phyllite-Quartzite Units, the Upper Trypali Unit and the Plattenkalk *s.l.* Unit. A detailed petrological and chemical description of these samples was conducted prior to selecting the most suitable ones for pseudosection modeling, Rb/Sr multi-mineral geochronology and (U-Th-Sm)/He thermochronology.

3.1 Electron Probe Microanalysis Data

Electron probe microanalyses were performed with a JEOL Superprobe JXA-8230 at GFZ Potsdam and a CAMECA SX-Five at Sorbonne Université using a 10-μm beam diameter, an accelerating voltage of 15 kV, a current intensity of 20 nA and a wavelength-dispersive spectroscopy mode. Standards used for the calibration are the following: orthoclase (Si, Al, K), rutile (Ti), Cr_2O_3 (Cr), hematite (Fe), rhodonite (Mn), periclase (Mg), wollastonite (Ca), albite (Na), celestine (Sr) and fluorite (F). The chemical compositions of key minerals constituting the main metamorphic parageneses were analyzed and their structural formulas were calculated following standard normalization procedures. For phengite, normalization was performed to 11 oxygen equivalents. For carpholite, normalization to 9 cations and 10 oxygen equivalents was applied, with Fe^{3+} estimated by charge balance and 11 wt.% H_2O included. Structural formulas for chloritoid and chlorite were calculated using *MinPlot* software (version 1.1) (*Walters*, 2022), with, chloritoid normalized to 8 cations and 12 oxygen equivalents and Fe^{3+} estimated by charge balance and chlorite normalized to 12 oxygen equivalents assuming all Fe as Fe^{2+}.

3.2 Pseudosection Modeling

P-T pseudosection modeling was carried out within the chemical system Na_2O-K_2O-FeO-MgO-Al_2O_3-SiO_2-H_2O-O_2 (NKFMASHO), following a free-energy minimization approach by using *Perple_X* software (version 7.0.9) (*Connolly*, 2005) and the self-consistent database of *Holland and Powell* (2011). Solid-solution models for white mica, chloritoid, chlorite and biotite are from *White et al.* (2014), while carpholite was modeled following *Smye et al.* (2010), garnet following *White et al.* (2005) and feldspar following *Fuhrman and Lindsley* (1988).

3.3 Rb/Sr Multi-mineral Geochronology

Rb/Sr isochron data are well suited to date mineral reactions and ductile deformation in white-mica-bearing metamorphic rocks. Indeed, deformation-induced recrystallisation of white mica together with associated phases (e.g., calcite, apatite) generally leads to complete Sr-isotopic re-equilibration and age resetting at temperatures <350 °C (*Müller et al.*, 1999). Accordingly, reset ages can be interpreted as reflecting the waning stage of deformation responsible for the last recrystallization event, considering that no later diffusive or retrogressive overprint occurred. Purely diffusional resetting of the Rb-Sr system in white mica is activated at temperatures of ~600 °C (*Villa*, 1998). Because the maximum recorded temperatures in the paleo-accretionary complex of western Crete are much lower; i.e., ~450-460 °C (*Menant et al.*, 2026, this issue), post-crystallization Rb and Sr diffusion process can be ruled out.

Samples for Rb/Sr multi-mineral dating were carefully selected based on microstructural and chemical criteria to solely record one crystallization or deformation event of interest. These samples were crushed and washed before carrying out mineral enrichment by magnetic and density separations, sieving and handpicking under the binocular microscope. The whole mineral-enrichment process and the chemical procedure for preparation of Rb and Sr are described in details in *Glodny et al.* (2008). Isotopic ratios were then determined on a Thermo Scientific TRITON thermal-ionization mass spectrometer at GFZ Potsdam. *Rb* isotope dilution analysis was done in static multicollection mode while *Sr* isotopic compositions were measured in dynamic multicollection mode. Data quality has been monitored by repeated analysis of $^{87}Sr/^{86}Sr$ of the NIST SRM 987 isotopic standard that yielded an average value of 0.710255 ± 0.000024 (2σ). For age calculations, standard errors of ±0.005% for $^{87}Sr/^{86}Sr$ and of ±1.5% for $^{87}Rb/^{86}Sr$ ratios were assigned to the results if individual analytical uncertainties were smaller than these values. Otherwise, individual analytical uncertainties were applied. The program ISOPLOT/EX 3.71 (*Ludwig*, 2008) was used for calculating regression lines. The ^{87}Rb decay constant as recommended by *Villa et al.* (2015) was used in all age calculations.

3.4 (U-Th-Sm)/He Thermochronology

(U-Th-Sm)/He thermochronology relies on the measurement of ^{4}He generated by the radioactive decay of ^{235}U, ^{238}U, ^{232}Th and ^{147}Sm. In rapidly cooled zircon crystals with low amounts of radiation damage, the closure temperature is ~120-180 °C (*Guenthner et al.*, 2013). The resulting ages are interpreted as reflecting the cooling of the zircon-bearing rock below this temperature range, providing valuable constraints on the timing of late exhumation and the thermal history of metamorphic complexes.

Selected samples were crushed and subjected to density separation. Zircons were then handpicked under binocular microscope. He extraction and measurement were performed at Universität Potsdam, using an ASI Alphachron He extraction and analysis system, equipped with a 30-W Coherent 978 nm diode laser and a Pfeiffer Prisma 200 Quadrupole mass spectrometer. Single-crystal zircon aliquots were heated with the laser system at 12 A for 10 minutes to ensure complete He release. The released gas was then purified by exposure to a hot getter (SAES AP10N) for 1 minute before analysis of ^{4}He by isotope dilution using a ^{3}He tracer, calibrated against a manometrically determined ^{4}He standard. Aliquots were re-extracted to verify complete He release. Following this, zircon aliquots were dissolved and U, Th and Sm were extracted for isotope analysis using a Thermo Element 2XR high-resolution ICP-MS instrument at GFZ Potsdam. Standard errors are typically $<1.5\%$ (2σ) for total U, between 1 and 5% (2σ) for ^{232}Th and between 1 and $>20\%$ (2σ) for ^{147}Sm. Further details on preparation and measurement procedures can be found in *Galetto et al.* (2021). The equation for estimating the fraction of helium retained in the crystal (F_{T}) was modified to include the broken crystal correction presented by *He and Reiners* (2022). The (U-Th-Sm)/He (ZHe) age of each sample was calculated by weighing the individual aliquots by the squared relative deviation (*Flowers et al.*, 2023), while errors are reported as the standard deviations of the ages.

4 Petrology and Mineral Chemistry

In this section, we report key petrological observations made on the tectono-metamorphic units recognized in western Crete (*Menant et al.*, 2026, this issue), as well as a detailed petrological and chemical characterization of rock samples that were collected and successfully analyzed for thermodynamic modeling and/or Rb/Sr multi-mineral geochronology (Table 1; see also Table S1 in Supporting Information). A description of additional samples that were also processed for dating purposes, but with less accurate age information, is provided in Supporting Information.

4.1 High-T Phyllite-Quartzite Unit

Chloritoid is commonly found in the phyllitic and impure quartzitic layers of the High-T Phyllite-Quartzite Unit that crops out in the northernmost part of the paleo-accretionary complex (Figure 1a). Carpholite, though reported locally in this area, is typically replaced by chloritoid (*Jolivet et al.*, 1996).

Sample CR2039 was collected from an outcrop consisting of marbles and phyllites displaying a moderately east-dipping foliation (Figure 2a). The phyllitic layers display a typical greenschist-facies paragenesis, comprising chlorite + epidote + phengite + paragonite + quartz + calcite ± rutile ± apatite (Figure 3a, Table 1). Phyllosilicates define the main foliation, while epidote forms syn-kinematic porphyroblasts associated with chlorite-rich pressure shadows. Epidote shows chemical zonation, with an allanite-rich core and an epidote-rich rim preserving a former foliation. The chemical composition of phengite is relatively homogeneous, with a low Si^{4+} content of 3.19-3.29 apfu and a muscovite content ranging from 74 to 79%, as determined from the ternary pyrophyllite-celadonite-muscovite diagram (Figure 4a, Tables 1, 2). Chlorite is dominated by the clinochlore and chamosite components, exhibiting a homogeneous X_{Mg} ratio ($X_{Mg} = Mg^{2+} / (Fe^{2+} + Mg^{2+})$) of 0.45-0.47 (Tables 1, 2).

An additional phyllite sample (CR1902b) was collected from this unit, showing the following paragenesis: chloritoid + phengite + paragonite + quartz ± apatite ± rutile. Further details on this sample are provided in Supporting Information.

4.2 Medium-T Phyllite-Quartzite Unit

The Medium-T Phyllite-Quartzite Unit is difficult to distinguish in the field from the High-T Phyllite-Quartzite Unit as they share similar lithologies and the same diagnostic HP-LT minerals dominated by chloritoid, although glaucophane-bearing metabasites are also locally observed (Figure 1a). Only the different maximum recorded temperatures estimated by the RSCM geothermometry provide clear evidence for a distinction between these two units; i.e., ~420-460 °C and ~390-415 °C for the High-T and Medium-T Phyllite-Quartzite Units, respectively (*Menant et al.*, 2026, this issue).

Sample CR1965b was collected close to the contact with the Upper Trypali Unit, from an outcrop exposing a deformed phyllite-quartzite alternation that locally exhibits a mylonitic fabric (Figure 2b). The phyllite-rich sample shows a blueschist-facies paragenesis with chloritoid + phengite + paragonite + chlorite + quartz ± dolomite-ankerite ± pyrite ± rutile ± apatite ± tourmaline (Figure 3b, Table 1). Phengite, paragonite and chloritoid mark the main foliation, although syn-kinematic chloritoid can also form radiating aggregates. Carbonate (dolomite-ankerite) is frequently fine-grained but partially-recrystallized large porphyroclasts are also reported (see inset of Figure 3b). Phengite has an intermediate Si^{4+} content of 3.28-3.38 apfu and a muscovite content mostly comprised between 60 and 70% (Figure 4b, Tables 1, 2). Composition of chloritoid is homogeneous with a low X_{Mg} ratio of 0.06-0.07, while chlorite (mainly chamosite) has a X_{Mg} ratio of 0.28-0.32.

Sample CR1925a comes from the central part of the Medium-T Phyllite-Quartzite Unit. It is an impure dolomitic marble cut by calcite-rich veins that exhibit the following paragenesis: phengite + paragonite + dolomite + quartz ± pyrite ± apatite (Table 1). Phengite shows a low Si^{4+} content of 3.09-3.18 apfu and a high muscovite content of 82-91% (Figure 4b, Tables 1, 2). Small pyrite crystals are typically replaced by goethite.

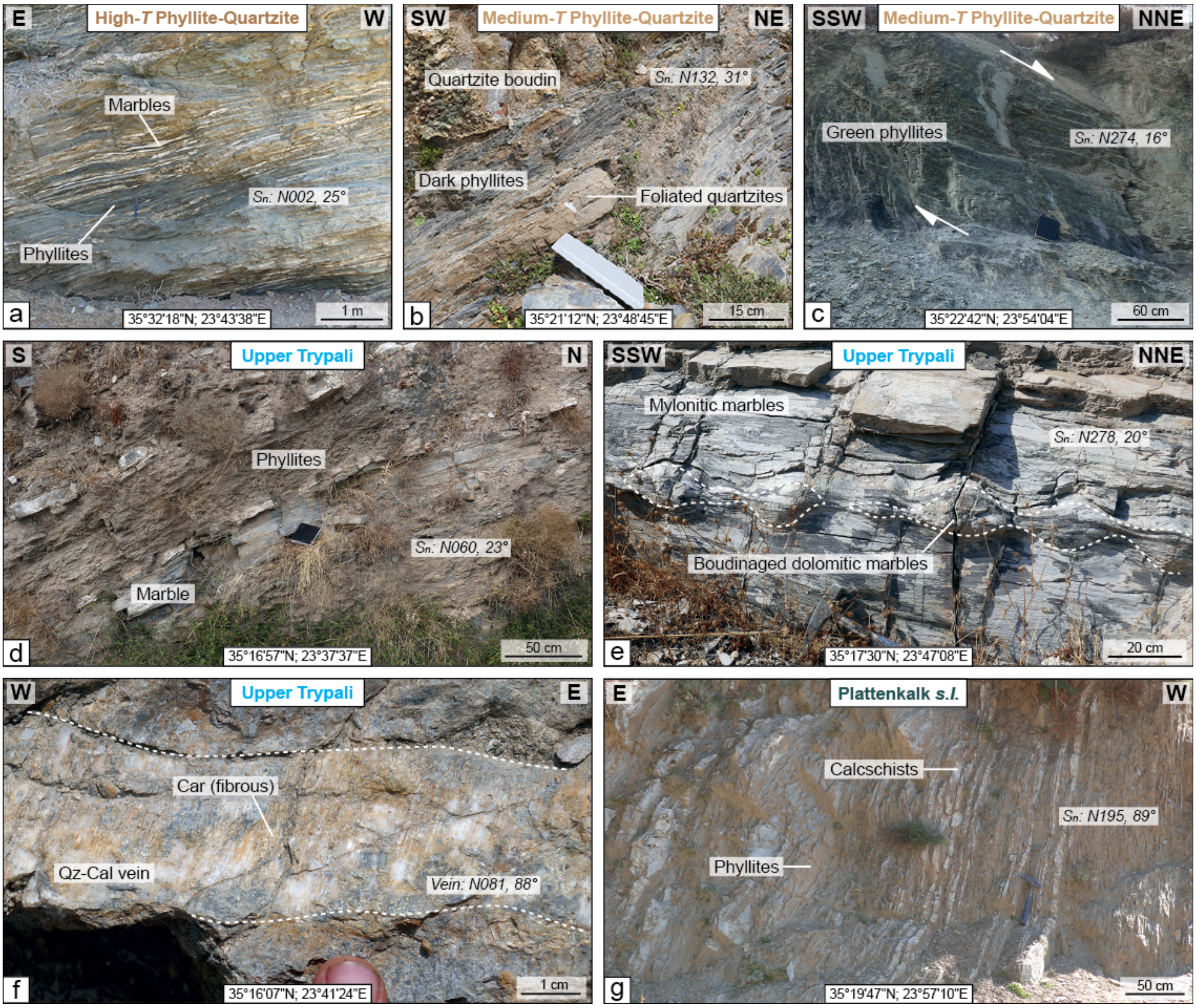

Figure 2 – Characteristic outcrops of the HP-LT units. Main foliation measurements (Sn) are reported according to the right-hand rule. (**a**) Phyllite and marble intercalations in the High-T Phyllite-Quartzite Unit (sample CR2039). (**b**) Phyllite and quartzite alternations in the Medium-T Phyllite-Quartzite Unit (sample CR1965b). (**c**) Top-to-the-NNE greenschist-facies shear zone in the Medium-T Phyllite-Quartzite Unit, in the hanging wall of the contact with the Upper Trypali Unit (sample CR1935b). (**d**) Phyllite and marble alternations in the Upper Trypali Unit (sample CR1920b). (**e**) Mylonitic marbles with calcschist intercalations in the Upper Trypali Unit, in the footwall of the contact with the Medium-T Phyllite-Quartzite Unit (sample CR1957b). (**f**) Carpholite-bearing, fibrous vein in the Upper Trypali Unit (near the collecting site of samples CR1945b and CR1945d). (**g**) Phyllite and calcschist intercalations in the Gigilos beds of the Plattenkalk *s.l.* Unit (samples CR2055a and CR2055b).

Sample CR1935b was collected from a top-to-the-NNE greenschist-facies shear zone located in the vicinity of the tectonic contact with the underlying Upper Trypali Unit (Figure 2c). The paragenesis observed in the phyllite-rich sample is chlorite + phengite + paragonite + albite + quartz + dolomite + calcite ± allanite ± rutile ± apatite (Figure 3c, Table 1). The phyllosilicates mark the main foliation, whereas albite forms porphyroclasts wrapped by the foliation. Phengite has a relatively high Si^{4+} content of 3.34-3.42 apfu and a relatively low muscovite content of 54-59% (Figure 4b, Tables 1, 2). Chlorite has a homogeneous X_{Mg} ratio of 0.52-0.54 and is mostly made of clinochlore and chamosite (Tables 1, 2).

4.3 Upper Trypali Unit

The Upper Trypali Unit exhibits HP-LT diagnostic minerals such as lawsonite and aragonite that are well expressed in phyllites and marbles, respectively (Figure 1a *Theye and Seidel*, 1993). Carpholite- and lawsonite-bearing veins exhibiting a fibrous texture are also commonly reported, while chloritoid and glaucophane are locally observed in phyllitic and metabasic layers, respectively.

Sample CR1920b is a quartzite alternating with phyllitic layers collected in the southwestern part of Crete, from an outcrop also exposing marble intercalations dipping moderately toward the SE (Figure 2b). It exhibits a blueschist-facies paragenesis

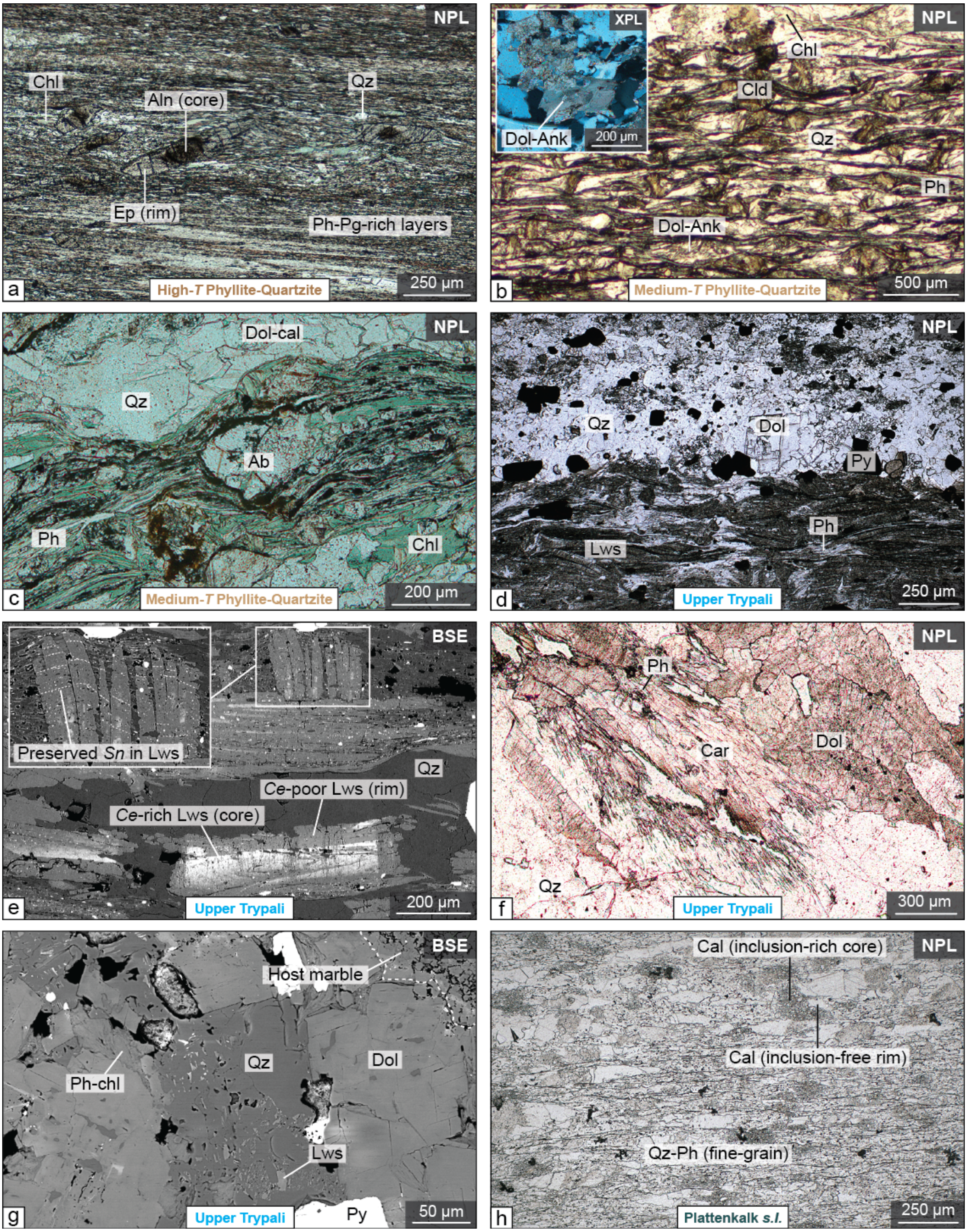

Figure 3 – Microscopic observations illustrating the main metamorphic parageneses. (**a**) Zoned epidote porphyroblasts with chlorite-rich pressure shadows in a phyllitic matrix (sample CR2039). (**b**) Radiating aggregate of chloritoid in a phengite-quartz-rich matrix (sample CR1965b). (**c**) Albite porphyroclasts in a phengite-chlorite-rich matrix (sample CR1935b). (**d**) Lawsonite porphyroblasts in phengite-rich layers alternating with quartz-rich layers (sample CR1920b). (**e**) Zoned lawsonite porphyroblasts aligned or superimposed on the main foliation (sample CR1920b). (**f**) Fibrous carpholite and elongated quartz and dolomite crystals in a H*P*-L*T* tensile vein (sample CR1945d). (**g**) Lawsonite inclusions in quartz crystals in a H*P*-L*T* tensile vein (sample CR2045b). (**h**) Zoned calcite porphyroblasts in a phengite-quartz-rich matrix (sample CR2055b). NPL: Non-polarized light. XPL: Cross-polarized light. BSE: Backscattered scanning electron microscopy image. Mineral abbreviations are after Whitney and Evans (2010).

Table 1 – Summary of petrological observations, chemical characteristics of key HP/LT minerals and Rb/Sr ages for selected samples from the HP-LT units.

Sample	Tectono-metamorphic unit	Main paragenesis	Si^{4+} (Ph, apfu)	X_{Mg} (Cph)	X_{Mg}	X_{Mg} (Chl)	Rb/Sr age (Ma)
CR2039	High-T Phyllite-Quartzite	Chl, Ep, Ph, Pg, Qz, Cal	3.19-3.29			0.45-0.47	16.4 ± 1.6
CR1965b	Medium-T Phyllite-Quartzite	Cld, Ph, Pg, Chl, Qz	3.28-3.39		0.06-0.07	0.28-0.32	20.8 ± 1.4
CR1925a	Medium-T Phyllite-Quartzite	Ph, Pg, Dol, Qz	3.09-3.18				24.3 ± 1.2
CR1935b	Medium-T Phyllite-Quartzite	Chl, Ph, Pg, Ab, Qz, Dol, Cal	3.34-3.42			0.52-0.54	15.75 ± 0.55
CR1920b	Upper Trypali	Lws, Ph, Pg, Qz, Dol	3.23-3.37				19.04 ± 0.76
CR1957b	Upper Trypali	Cal, Ph, Qz	3.17-3.24				16.59 ± 0.25
CR2073	Upper Trypali	Cal, Ph, Qz	3.09-3.13				16.74 ± 0.37
CR1917b	Upper Trypali	Car, Ph, Pg, Qz, Arg, Dol	3.28-3.32	ca. 0.80			14.66 ± 0.68
CR1945d	Upper Trypali	Car, Ph, Pg, Qz, Dol	3.22-3.26	0.71-0.74			15.5 ± 1.2
CR1945b (vein)	Upper Trypali	Lws, Ph, Pg, Chl, Qz, Dol	3.20-3.25			0.77-0.79	17.02 ± 0.50
CR1945b (host)	Upper Trypali	Ph, Dol	3.21-3.27				16.1 ± 4.6
CR2055b	Plattenkalk s.l.	Ph, Chl, Cal, Qz	3.28-3.41			0.46-0.54	41.79 ± 0.66

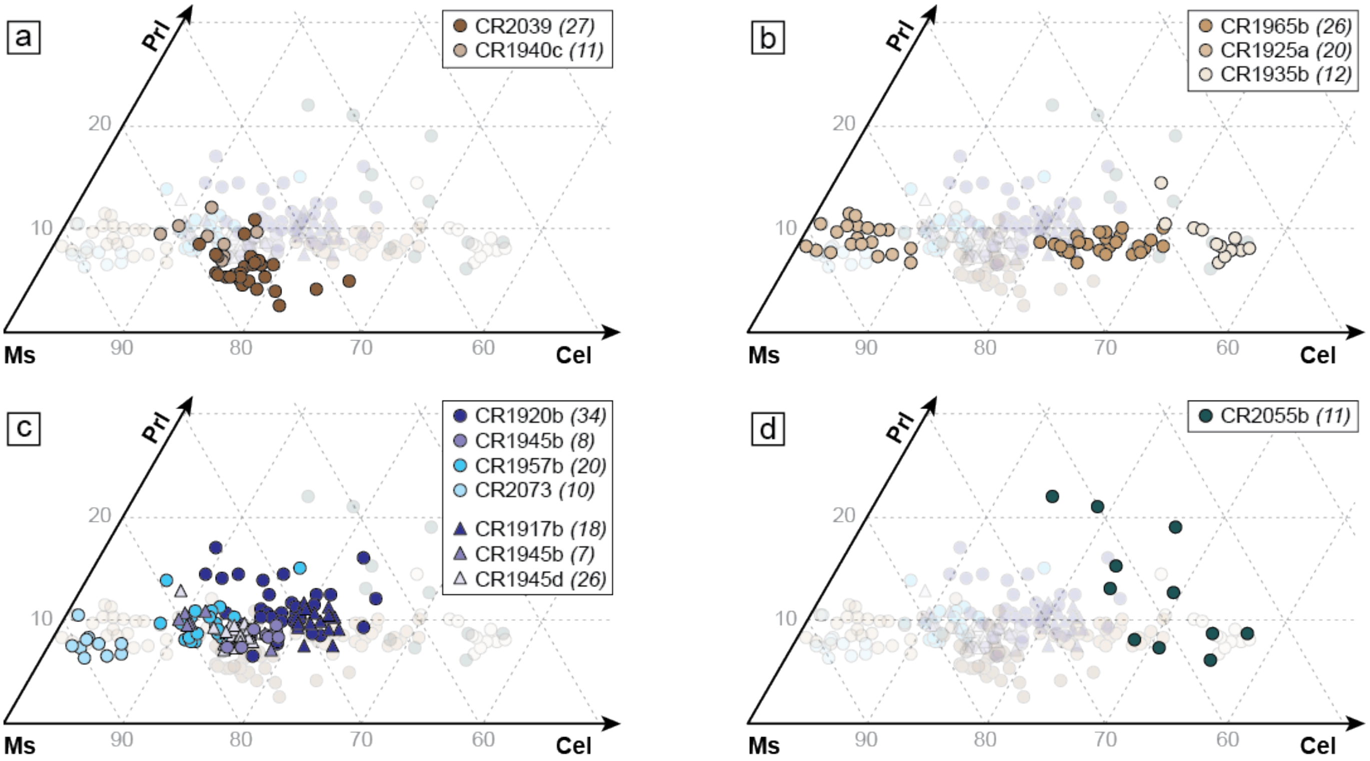

Figure 4 – Ternary plots of phengite compositions from the (**a**) High-T Phyllite-Quartzite Unit, (**b**) Medium-T Phyllite-Quartzite Unit, (**c**) Upper Trypali Unit and (**d**) Plattenkalk *s.l.* Unit. Symbols in transparency represent the full dataset. The number of electron probe microanalyses is shown in italics.

with lawsonite + phengite + paragonite + quartz + dolomite ± chlorite ± pyrite ± rutile ± apatite (Figure 3d, Table 1). The foliation is marked by the planar alignment of phengite and lawsonite, although the latter can also be expressed as post-kinematic radiating porphyroblasts with numerous inclusions outlining the main foliation. Lawsonite is often zoned with a *Ce*-rich core and a *Ce*-poor rim (Figure 3e). Phengite has a moderately variable Si^{4+} content of 3.23-3.37 apfu and a muscovite content mostly comprised between 65 and 75% (Figure 4c, Tables 1, 2). Pyrite is common and often partly replaced by hematite.

Sample CR1957b is a strongly deformed impure calcschist collected in the footwall of the tectonic contact between the Medium-T Phyllite-Quartzite and Upper Trypali Units (Figure 2e). The calcschist exhibits a shallow dipping mylonitic fabric that commonly wraps transposed and boudinaged dolomitic veins. The main paragenesis is calcite + phengite + quartz ± paragonite ± pyrite ± rutile ± apatite (Table 1). At microscopic scale, the mylonitic foliation is mostly marked by fine-grained phengite layers. Phengite has a relatively low Si^{4+} content of 3.17-3.24 and a muscovite content of 75-82%, with one notable exception exhibiting a Si^{4+} content of 3.34 and a muscovite content of 67%. Fine-grained pyrite is well expressed in phyllosilicate layers and commonly exhibits a corona texture witnessing partial oxidation in goethite.

Table 2 – Representative probe microanalysis data of key HP/LT minerals for selected samples. P-Q: Phyllite-Quartzite.

Mineral	**Phengite**											
Unit	**High-*T* P-Q**	**Medium-*T* P-Q**			**Upper Trypali**							**Plattenkalk *s.l.***
Sample	**CR2039**	**CR1965b**	**CR1925a**	**CR1935b**	**CR1920b**	**CR1957b**	**CR2073**	**CR1917b**	**CR1945d**	**CR1945b (vein)**	**CR1945b (host)**	**CR2055b**
SiO_2	46.82	49.89	46.88	49.94	48.83	48.60	46.97	49.22	48.70	48.60	48.85	50.40
TiO_2	0.16	0.13	0.04	0.34	0.04	0.09	0.12	0.07	0.05	0.01	0.06	0.13
Al_2O_3	30.12	30.06	35.98	26.41	31.20	34.05	35.80	30.53	32.84	34.27	32.11	27.33
FeO_T	4.41	2.46	0.72	4.74	0.06	0.00	0.02	0.55	0.69	0.25	0.47	2.46
MnO	0.06	0.00	0.00	0.01	0.00	0.00	0.00	0.00	0.04	0.00	0.03	0.04
MgO	1.54	1.83	0.37	2.76	2.89	1.60	1.14	2.59	1.69	1.28	1.98	3.08
CaO	0.00	0.03	0.05	0.01	0.06	0.02	0.26	0.14	0.06	0.10	0.20	0.09
Na_2O	0.66	0.33	0.75	0.32	0.50	0.56	0.72	0.52	0.62	0.96	0.61	0.15
K_2O	9.61	10.12	9.59	10.31	9.73	9.82	9.76	9.98	9.81	9.26	9.84	10.68
Sum	93.38	94.86	93.72	94.84	93.30	94.75	94.80	93.61	94.50	94.73	94.16	94.37
Si	3.22	3.33	3.14	3.39	3.33	3.21	3.10	3.30	3.24	3.20	3.26	3.40
Ti	0.01	0.01	0.00	0.02	0.00	0.00	0.01	0.00	0.00	0.00	0.00	0.01
Al	2.44	2.37	2.79	2.11	2.40	2.65	2.79	2.42	2.57	2.66	2.52	2.17
Fe^{2+}	0.25	0.14	0.04	0.27	0.00	0.00	0.00	0.03	0.04	0.01	0.03	0.14
Fe^{3+}	0.00	0.00	0.00	0.00	0.00	0.00	0.00	0.00	0.00	0.00	0.00	0.00
Mn	0.00	0.00	0.00	0.00	0.00	0.00	0.00	0.00	0.00	0.00	0.00	0.00
Mg	0.16	0.18	0.04	0.28	0.31	0.16	0.11	0.26	0.17	0.13	0.20	0.31
Ca	0.00	0.00	0.00	0.00	0.00	0.00	0.01	0.01	0.00	0.01	0.01	0.01
Na	0.09	0.04	0.10	0.04	0.04	0.07	0.09	0.07	0.08	0.12	0.08	0.02
K	0.84	0.86	0.82	0.89	0.84	0.83	0.82	0.85	0.83	0.78	0.84	0.92

Mineral	**Carpholite**		**Chloritoid**	**Chlorite**				
Unit	**Upper Trypali**		**Medium-*T* P-Q**	**High-*T* P-Q**	**Medium-*T* P-Q**		**Upper Trypali**	**Plattenkalk *s.l.***
Sample	**CR1917b**	**CR1945d**	**CR1965b**	**CR2039**	**CR1965b**	**CR1935b**	**CR1945b (vein)**	**CR2055b**
SiO_2	38.79	38.87	23.88	24.65	24.10	26.80	30.66	27.62
TiO_2				0.06	0.05	0.04	0.00	0.08
Al_2O_3	32.66	32.63	39.92	21.81	22.07	20.39	25.18	20.32
FeO_T	4.49	6.08	26.89	26.71	33.49	24.43	9.56	22.80
MnO	0.06	0.09	0.13	0.11	0.01	0.10	0.01	0.11
MgO	10.28	9.34	1.02	12.87	8.13	15.76	19.70	12.27
CaO	0.03	0.01	0.03	0.02	0.02	0.03	0.11	0.26
Na_2O	0.04	0.00	0.00	0.03	0.00	0.00	0.03	0.05
K_2O	0.15	0.02	0.00	0.03	0.00	0.00	0.62	0.76
Sum	86.49	87.05	91.87	86.29	87.87	87,55	85.87	84.27
Si	2.05	2.06	2.00	2.66	2.65	2.80	3.00	3.00
Ti				0.00	0.00	0.00	0.00	0.01
Al	2.04	2.04	3.96	2.78	2.85	2.52	2.90	2.60
Fe^{2+}	0.20	0.27	1.87	2.41	3.07	2.14	0.78	2.07
$Fe3^{3+}$	0.00	0.00	0.02	0.00	0.00	0.00	0.00	0.00
Mn	0.00	0.00	0.01	0.01	0.00	0.01	0.00	0.01
Mg	0.81	0.74	0.13	2.07	1.33	2.46	2.87	1.99
Ca	0.00	0.00	0.00	0.00	0.00	0.00	0.00	0.00
Na	0.01	0.00	0.00	0.00	0.00	0.00	0.00	0.00
K	0.02	0.00	0.00	0.00	0.00	0.00	0.00	0.00

Sample CR2073 is a mylonitic calcschist coming from the footwall of the top-to-the-S detachment that juxtaposes the low-grade Gavrovo-Tripolitza Unit on top of the HP-LT nappe stack (Menant *et al.*, this volume). The sample has a similar paragenesis as CR1957b, although it contains phengite with a lower Si^{4+} content (3.09-3.13 apfu) and a higher muscovite content (86-90%; Figure 4c, Tables 1, 2).

Samples CR1917b, CR1945d and CR1945b are cm-thick tensile veins with a fibrous texture that were collected from two locations in the southwestern and southern parts of the study area (Figures 1a, 2f). CR1917b is composed of Mg-carpholite + phengite + paragonite + quartz + aragonite + dolomite (Table 1). This vein is locally crosscut by cracks filled with calcite and phengite. Phengite has a homogenous Si^{4+} content of 3.28-3.32 apfu and a muscovite content of 67-71%, while Mg-carpholite shows a constant X_{Mg} ratio of ~0.80 (Figure 4c, Tables 1, 2). CR1945d is also a carpholite-bearing vein with the following mineral content: Mg-carpholite + phengite + paragonite + quartz + dolomite ± rutile (Figure 3f). Chlorite is also locally observed in late cracks. Measured Si^{4+} content of phengite is homogenous (3.22-3.26 apfu) with a 74-78% muscovite content (Figure 4c, Tables 1, 2). Mg-carpholite exhibits a moderate to high X_{Mg} ratio of 0.71-0.74. Both the vein and the host marble were analyzed from sample CR1945b. The vein consists of lawsonite + phengite + paragonite + chlorite + quartz + dolomite ± pyrite ± apatite with lawsonite expressed as inclusions in quartz crystals (Figure 3g), whereas the host comprises phengite + dolomite ± pyrite (Table 1). Dolomite grains in the host are zoned, reflecting variation of the FeO content between 0 and ~6%. Pyrite is partly oxidized as attested by the corona texture. Importantly, some phengite flakes are continuous from the host to vein, suggesting that the hosting metamorphic paragenesis is, at least, partly coeval with the vein formation. Accordingly, phengite in the vein and the host exhibits a similar Si^{4+} content of 3.20-3.25 apfu and 3.21-3.27 apfu and a relatively high muscovite content of 74-80% and 72-77%, respectively (Figure 4c, Tables 1, 2). Chlorite in the veins (mainly sudoite) has a high X_{Mg} ratio of 0.77-0.79.

An additional phyllitic sample (CR1918a) was collected from the Upper Trypali Unit. This sample is similar as CR1920b, although more phyllitic, and exhibits the following paragenesis: lawsonite + phengite + paragonite + chlorite + quartz + dolomite ± pyrite ± rutile ± apatite. Further details on this sample are provided in Supporting Information.

4.4 Plattenkalk *s.l.* Unit

So far, no diagnostic minerals for a H*P*-L*T* event have been reported in the Plattenkalk *s.l.* Unit in western Crete. However, the local occurrence of carpholite in metabauxites of central Crete and phyllites of Peloponnese demonstrates that this unit was affected by subduction-related metamorphism (*Seidel et al.*, 1982; *Blumör et al.*, 1994).

Sample CR2055b is a calcschist from the Gigilos beds, i.e., a siliciclastic formation intercalated between the Mavri dolomitic formation and the typical, chert-bearing, platy carbonates of the Plattenkalk *s.s.* series. At outcrop scale, calcschists are interlayered with phyllites and show a sub-vertical layering that marks the core of a regional-scale anticline exposing the deepest part of the metamorphic nappe stack in western Crete (Figures 1a, 2g). The paragenesis consists of zoned-calcite porphyroblasts with inclusion-rich cores in a fine-grained matrix of phengite + quartz + chlorite ± hematite ± titanite ± apatite (Figure 3h, Table 1). Phengite has a high and heterogenous Si^{4+} content of 3.28-3.41 and a relatively low muscovite content of 50-63% (Figure 4d, Tables 1, 2). Chlorite is dominated by clinochlore and chamosite and exhibits a X_{Mg} ratio of 0.46-0.54.

One additional sample (CR2055a) was collected from the same outcrop, exhibiting a similar paragenesis as sample CR2055b. Further details on this sample are provided in Supporting Information.

5 *P-T* Constraints

A *P-T* pseudosection was calculated for the chloritoid-rich phyllite sample CR1965b, considered representative of the phyllitic layers of the Medium-*T* Phyllite-Quartzite Unit that is largely exposed in the study area (Figure 1; Table 1). The bulk composition estimate for this sample was derived from a careful appraisal of the modal proportions and representative chemical composition of the mineral phases in the main paragenesis. Fe_2O_3 was considered negligible due to (i) the low degree of retrogression, which indicates minimal re-equilibration under more oxidizing shallow-crustal conditions and (ii) the presence of pyrite and absence of hematite in the peak metamorphic paragenesis. Additionally, the CaO component was excluded from the thermodynamic calculation because the lack of robust constraints on the amount of CO_2 in the system prevents a reliable estimate of the stability conditions for carbonates (i.e., the only Ca-bearing mineral phase in sample CR1965b). This simplification is justified, as we assume local equilibrium within a microvolume where the observed modal proportion of carbonate is low (<5%). The model was set to 250-500 °C and 0.8-2.0 GPa, assuming water-saturated conditions that are supported by the widespread occurrence of hydrated minerals such as phengite, chloritoid and chlorite in the sample.

The best-fit *P-T* conditions of ~15-17 kbar and 390-440 °C is obtained (Figure 5), considering the main paragenesis (Table 1), the Si^{4+} content in phengite (3.28-3.38 apfu) and the X_{Mg} ratio of chloritoid (0.06-0.07). The temperature estimate falls in the range of the maximum recorded temperatures estimated for the Medium-*T* Phyllite-Quartzite Unit, using the RSCM method (~390-420 °C) (Menant *et al.*, this volume), implying that the mineral assemblage of sample CR1965b was stable close to the peak metamorphic temperature. There is also a general agreement between the calculated mineral proportions at 16 kbar, 400 °C and the modal mineral abundance observed in thin section, with the exception of the carbonates that were excluded from the pseudosection modeling (compare the two pie charts in Figure 5). It is also worth mentioning that the ~0.42 X_{Mg} ratio of chlorite, estimated for the best-fit *P-T* conditions, is significantly higher than the one measured in thin section (0.28-0.32; Table 1), suggesting that this mineral was probably re-equilibrated during the retrograde path.

A similar thermodynamic modeling approach was carried out for a phyllite-rich sample (CR1918a) belonging to the underlying Upper Trypali Unit. Further details on the calculated *P-T* pseudosection are provided in Supporting Information.

6 Rb/Sr-dating Results

Rb/Sr isochron data of 12 samples, from the top to the base of the H*P*-L*T* nappe stack, provide well-constrained age information described hereafter (Figures 6, 7a-b). Additional Rb/Sr isochron plots, as well as the complete analytical dataset, are presented in Supporting Information.

In the High-*T* Phyllite-Quartzite Unit, an epidote-bearing phyllite (sample CR2039) yields an age of 16.4 ± 1.6 Ma with a relatively high mean squared weighted deviation (MSWD = 13) from a seven-point regression line, excluding apatite (Figure 6a). Indeed, apatite plots significantly below the regression line, likely indicating a *Sr*-isotopic disequilibrium for this mineral. Nonetheless, the isotopic consistency between the two low-Rb/Sr calcite fractions and the four white-mica fractions (separated according to grain size, with the 90-63-μm white-mica fraction analyzed twice) supports the accuracy of the isochron data.

The oldest well-constrained age in the Medium-*T* Phyllite-Quartzite Unit is from a dolomitic marble (sample CR1925a) that produces an age of 24.3 ± 1.2 Ma (MSWD = 8; Figure 6b) using a five-point regression line excluding unequilibrated colorless calcite. In this sample, calcite is expressed as late veins that locally crosscut the main foliation and, therefore, postdate the main crystallization event recorded by the isochron data. A chloritoid-bearing phyllite (sample CR1965b)

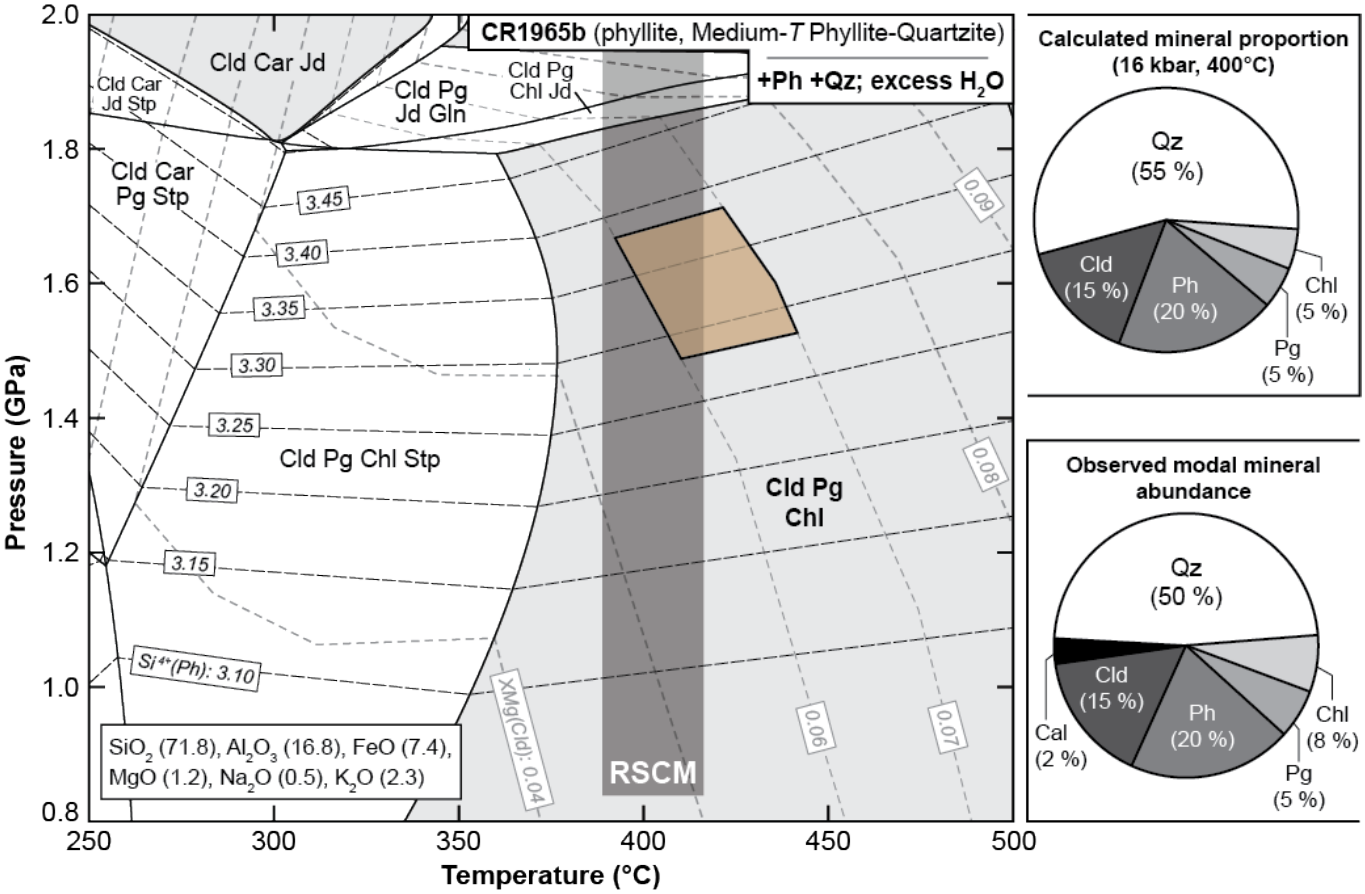

Figure 5 – *P-T* pseudosection in the NKFMASHO system for sample CR1965b (Medium-*T* Phyllite-Quartzite Unit), highlighting the best-fit area (brown domain) based on observed paragenesis and mineral composition. The RSCM temperature range for this unit is from Menant *et al.* (this volume). Calculated volume proportions and observed modal abundances of the main minerals are represented in insets. Mineral abbreviations are after *Whitney and Evans* (2010).

yields a seven-point regression line corresponding to an age of 20.8 ± 1.4 Ma (MSWD = 4; Figure 6c). Because carbonate fractions plot in a scattered manner and considering the partial recrystallization of large carbonate porphyroclasts observed at microscopic scale (Figure 3b), this mineral likely exhibits a *Sr*-isotopic disequilibrium and is, consequently, excluded from the calculation data. It is, however, noteworthy that the isochron age including the carbonate fractions does not differ significantly, although the MSWD is higher (22.8 ± 2.7 Ma, MSWD = 82). A sensibly younger age is obtained from sample CR1935b that exhibits a typical greenschist-facies assemblage (15.75 ± 0.55 Ma, MSWD = 40; Figures 3c, 6d). In the isochron diagram, the >250-μm mica fraction plots above the regression line for the five other phases, indicating a *Sr*-isotopic disequilibrium likely related to the partial reset of large white-mica flakes during the greenschist-facies retrogression event.

Seven well-constrained Rb/Sr multimineral ages are from the Upper Trypali Unit. A lawsonite-bearing phyllite (sample CR1920b; Figure 3d) yields a four-point isochron including lawsonite that corresponds to a robust age of 19.04 ± 0.76 Ma (MSWD = 0.62; Figure 6e). Mylonitic calcschists from samples CR1957b and CR2073 provides similar ages of 16.59 ± 0.25 Ma (MSWD = 0.23) and 16.74 ± 0.37 Ma (MSWD = 5), respectively (Figure 6f-g). Two carpholite-bearing veins from the same unit yield younger ages of 14.66 ± 0.68 Ma (MSWD = 2.5, samples CR1917b; Figure 6h) and 15.5 ± 1.2 Ma (MSWD = 18, sample CR1945d; Figure 6i), with the CR1917b isochron defined by the alignment of aragonite and carpholite-white mica fractions along a seven-point regression line. Another isochron diagram characterized by a six-point regression line indicates a 17.02 ± 0.50 Ma crystallization age (MSWD = 5.3) for a lawsonite-bearing vein (sample CR1945b; Figure 6j). A consistent, but less well-constrained, age of 16.1 ± 4.6 Ma (MSWD = 111; Figure 6k) was also obtained for the host marble coming from the same sample.

Finally, the oldest age obtained in this study comes from sample CR2055b, a calcschist belonging to the Gigilos beds that is part of the Plattenkalk *s.l.* Unit. This age of 41.79 ± 0.66 Ma (MSWD = 21; Figure 6l) is calculated from a 7-point isochron that does not show any obvious isotopic disequilibrium.

7 (U-Th-Sm)/He Thermochronological Results

Four samples were collected between 345 and 590 m in elevation from coarse-grained metaclastic layers belonging to the High-*T* and Medium-*T*

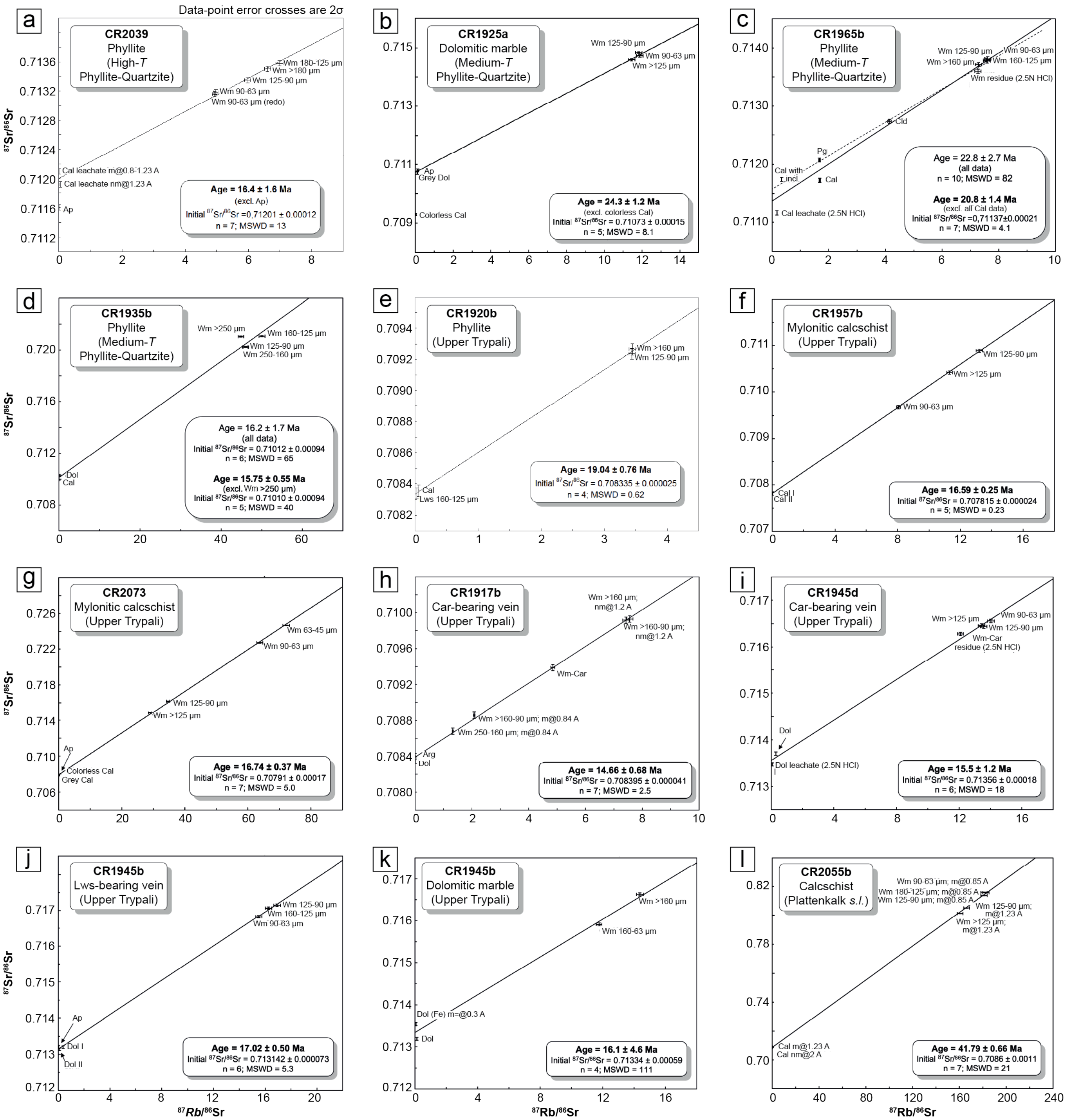

Figure 6 – (**a-l**) Rb/Sr isochron diagrams for the H*P*-L*T* units. MSWD: Mean square weighted deviation. Mineral abbreviations are after *Whitney and Evans* (2010).

Phyllite-Quartzite Units. Samples CR2044, CR2062 and CR2066 are poorly to moderately deformed quartzites made of large quartz porphyroclasts in a fine-grained matrix of quartz and phengite, whereas sample CR2069 consists of moderately deformed calcite and quartz porphyroclasts associated with chloritoids, phengite and scarce chlorite. More information regarding the geographic position and the petrological and textural description of these samples is provided in Supporting Information.

Samples CR2044 and CR2066 yield tightly clustered single crystal dates, whereas CR2062 and CR2069 exhibit over-dispersed dates, defined as a >15% (1σ) standard error of the mean age (Table 3) (Flowers *et al.*, 2023). The ZHe closure temperature can vary depending on both crystal size and radiation damage, which may help explain the over-dispersed ages. However, the zircons in this study have relatively low effective uranium concentrations ([U]e) and cooled from high temperatures during the Miocene, suggesting that radiation damage is minimal (Guenthner *et al.*, 2013) and should not cause significant variation in the closure temperature. Additionally, the relationship between effective spherical radius (ESR) and single-grain age does not account for the over-dispersed pattern (Figure 8a). Therefore, for

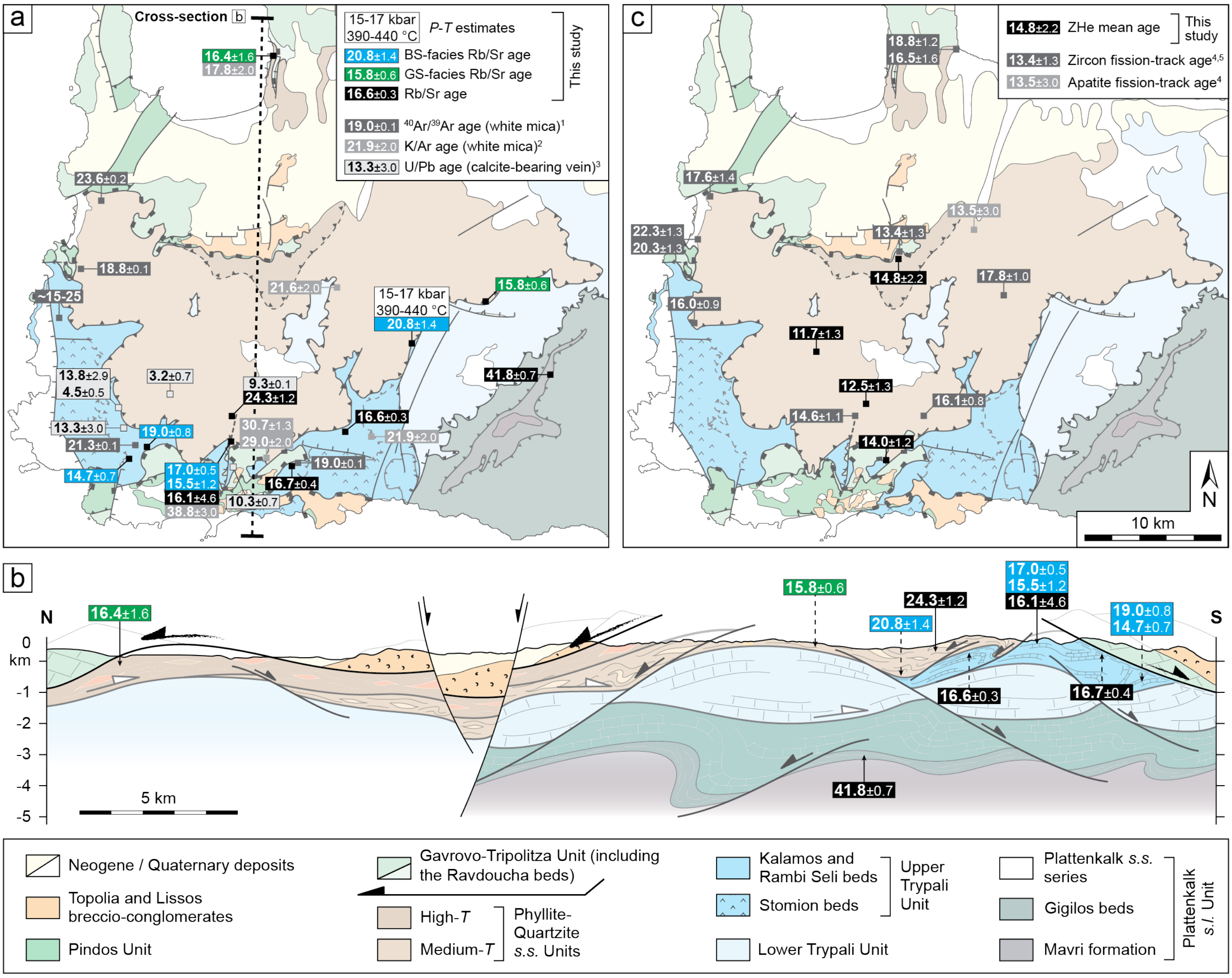

Figure 7 – Temporal constraints on the H*P*-L*T* duplex from this study and the literature. (**a**) Synthesis of geochronological ages and *P-T* thermobarometric estimate. BS: blueschist. GS: greenschist. (b) Synthetic cross-section of western Crete with Rb/Sr multimineral ages from this study. (**c**) Synthesis of low-temperature thermochronological ages. (1) *Jolivet et al.* (1996); (2) *Seidel et al.* (1982); (3) *Ring et al.* (2022); (4) *Thomson et al.* (1998); (5) *Marsellos et al.* (2010).

these two samples, we selected the largest number of grains that yields a population without over-dispersion.

Sample CR2062 was collected at ~150 m below the top-to-the-N detachment that marks the northern edge of the H*P*-L*T* nappe stack. Six single-crystal zircon aliquots were separated and analyzed. Aliquots #2 and #4 yielded no gas and are not discussed further. The remaining four crystals yielded ZHe single-grain ages ranging from 11.0 ± 0.2 Ma to 17.6 ± 0.3 Ma, with a mean age of 14.8 ± 2.2 Ma based on three aliquots (Figure 8b; Table 3). Sample CR2066, located at a high elevation (590 m) in the central part of the metamorphic dome, had six zircon aliquots processed. The ZHe single-grain ages ranged from 11.0 ± 0.1 Ma to 14.9 ± 0.3 Ma, with a mean age of 11.7 ± 1.3 Ma. Sample CR2069 was collected from the central part of the metamorphic dome at a lower elevation (345 m). Six zircon aliquots yielded over-dispersed ZHe single-grain ages ranging from 11.2 ± 0.1 Ma to 23.2 ± 0.8 Ma, with a poorly constrained mean age of 13.4 ± 4.2 Ma. Sample CR2044, collected from the lowermost section of the Medium-*T* Phyllite-Quartzite Unit at the southern edge of the metamorphic nappe stack, is located ~50 m below the top-to-the-S detachment. Six zircon aliquots yielded ZHe ages ranging from 11.7 ± 0.1 Ma to 15.1 ± 0.1 Ma, with a mean age of 14.0 ± 1.2 Ma.

In summary, the mean ZHe ages do not correlate with the elevation but show a consistent decrease from the northern and southern edges of the H*P*-L*T* duplex toward its center (Figure 8b). It is also worth noting that the oldest mean ZHe age was obtained from the High-*T* Phyllite-Quartzite Unit; i.e., the uppermost tectono-metamorphic unit of the H*P*-L*T* nappe pile in western Crete.

8 Discussion

Petrological observations, thermodynamic calculations and geochronological and low-*T* thermochronological dating presented in this study are combined with data from the literature to reconstruct the *P-T-t* paths of the H*P*-L*T* units forming the paleo-accretionary duplex

Table 3 – ZHe thermochronology results. [U]e: effective uranium concentration calculated after *Flowers et al.* (2023). F_T: fraction of helium retained in the crystal after *He and Reiners* (2022). ESR: effective spherical radius. Crystal shape: r = rounded, 2 and 1 denote euhedral crystal with 2- and 1-terminations, respectively. P-Q: Phyllite-Quartzite. Analyses in italics were excluded from the mean-age calculation (see Section 8.2).

Sample	Unit	Elevation (m)	Zircon number	U (ppm)	Th (ppm)	Sm (ppm)	Th/^{238}U	He (nmol/g)	Mass (μg)	[U]e (ppm)	FT	ESR (μm)	Crystal shape	FT-corrected age (Ma)	Mean age (Ma)
CR2062	High-*T* P-Q	508	#1	169.0	49.3	0.6	0.3	10.9	14.74	180.7	0.86	79.6	2	13.1 ± 0.2	14.8 ± 2.2
			#2						20.42			98.5	r		
			#3	27.3	38.7	0.3	1.5	2.6	14.25	36.5	0.85	84.2	r	15.3 ± 0.3	
			#4						6.91			69.0	r		
			#5	93.1	83.0	0.5	0.9	8.9	11.37	112.8	0.84	72.7	2	17.4 ± 0.3	
			#6	76.0	62.1	0.3	0.8	4.5	9.83	90.8	0.84	76.2	r	11.0 ± 0.2	
CR2066	Medium-*T* P-Q	590	#1	175.4	84.0	0.6	0.5	10.2	32.93	195.4	0.88	102.0	r	11.0 ± 0.1	11.7 ± 1.3
			#2	36.8	16.6	0.1	0.5	2.4	20.00	40.8	0.88	100.6	r	12.4 ± 0.2	
			#3	363.6	87.6	0.2	0.2	24.2	6.41	384.4	0.80	57.0	2	14.6 ± 0.3	
			#4	185.0	123.2	0.5	0.7	11.2	14.39	214.3	0.86	87.8	r	11.2 ± 0.1	
			#5	134.4	125.1	0.8	1.0	9.8	15.02	164.2	0.86	88.0	r	12.9 ± 0.1	
			#6	147.2	143.8	0.6	1.0	10.8	13.64	181.4	0.86	84.6	r	12.9 ± 0.4	
CR2069	Medium-*T* P-Q	345	#1	110.8	26.4	0.3	0.2	7.4	14.74	117.1	0.85	76.5	2	13.9 ± 0.4	13.4 ± 4.2 (12.5 ± 1.3 after data curation)
			#2	208.5	57.1	0.2	0.3	14.4	12.34	222.1	0.86	81.7	r	14.0 ± 0.2	
			#3	125.6	104.4	0.2	0.9	10.6	11.72	150.4	0.83	69.3	2	15.8 ± 0.2	
			#4	292.4	177.1	0.8	0.6	18.5	5.00	334.6	0.79	54.5	2	13.0 ± 0.2	
			#5	142.6	142.6	1.3	1.0	8.4	4.18	176.6	0.78	55.8	r	11.2 ± 0.1	
			#6	136.0	71.1	0.2	0.5	16.5	18.34	153.0	0.86	74.9	1	23.2 ± 0.8	
CR2044	Medium-*T* P-Q	556	#1	65.1	72.7	0.3	1.2	5.5	22.12	82.4	0.86	85.0	2	14.5 ± 0.1	14.0 ± 1.2
			#2	120.6	37.5	1.0	0.3	8.0	15.94	129.6	0.85	74.0	2	13.5 ± 0.1	
			#3	152.7	34.9	0.1	0.2	8.6	17.71	161.1	0.86	81.1	2	11.6 ± 0.1	
			#4	172.6	91.3	0.1	0.5	12.7	30.86	194.3	0.89	111.1	r	13.5 ± 0.7	
			#5	17.8	11.1	0.3	0.6	1.3	8.41	20.5	0.81	59.6	2	14.3 ± 0.4	
			#6	111.3	111.3	0.3	1.2	9.5	11.02	142.6	0.83	67.8	2	14.9 ± 0.1	

of western Crete. The revised tectono-metamorphic evolution of the Crete-Peloponnese metamorphic belt illuminates the temporal succession of basal-accretion events along the Hellenic subduction zone during the Oligocene to Miocene, providing key constraints for the regional geodynamics and for the tectonic monitoring of deep mass-flux events along active margins worldwide.

8.1 Contrasted *P*-*T* Records Throughout the Nappe Stack

A minimum of five tectono-metamorphic units are identified in western Crete, based on distinct maximum recorded temperatures estimated using RSCM geothermometry (Menant *et al.*, this volume); i.e., from top to bottom, the High-*T* and Medium-*T* Phyllite-Quartzite Units (~420-460 °C and ~390-415 °C, respectively), the Upper and Lower Trypali Units (~360-390 °C and ~320-330 °C) and the Plattenkalk *s.l.* Unit (~340-350 °C). These contrasting thermal histories during the Alpine subduction event are further revealed through the mapping of H*P*-L*T* index minerals (Figure 1). In the High-*T* and Medium-*T* Phyllite-Quartzite Units, chloritoid is abundant, often replacing Mg-carpholite that typically appears as pseudomorphs (Figure 3b) (Jolivet *et al.*, 1996). This is consistent with temperature exceeding ~400 °C at the pressure-peak to early retrograde stage (*Vidal et al.*, 1992; *Trotet et al.*, 2006; *Pourteau et al.*, 2014). More precise *P*-*T* estimates for the High-*T* Phyllite-Quartzite Unit suggest peak conditions of 17-18 kbar and 410-430 °C (Figure 1b) ("Xania" sample in *Jolivet et al.*, 1996), supported by the RSCM temperatures ranging between 420 and 460 °C (Figure 9a).

For the Medium-*T* Phyllite-Quartzite Unit, calculated *P*-*T* conditions (15-17 kbar and 390-440 °C; Figure 5) are consistent with earlier estimates ("Sfinari" sample in Jolivet *et al.* (1996)), except that the pressure is slightly lower, likely reflecting the onset of the retrograde stage, characterized by a near isothermal decompression (Figure 9a) (*Theye et al.*, 1992; *Jolivet et al.*, 1996).

Structurally deeper, the Upper Trypali Unit preserves carpholite in tensile veins, along with widespread lawsonite and aragonite in phyllite-rich and carbonate-rich layers, respectively (Figures 1, 3d-f) (*Theye and Seidel*, 1993). This mineral assemblage suggests lower temperatures than the overlying units, supported by RSCM temperatures of 360-390 °C (*Menant et al.*, 2026, this issue). Consistent *P*-*T* constraints of 16-18 kbar and 360-410 °C were obtained for this unit ("Agio Theodori" and "Prodomi" samples in *Jolivet et al.*, 1996), although no distinction from the Phyllite-Quartzite Units was made (Figures 1b, 9a). Our study provides a *P*-*T* pseudosection for a lawsonite-bearing phyllite, yielding a pressure range of 8-16 kbar that does not allow constraining more accurately the peak metamorphic conditions for this unit (see Supporting Information). The preservation of aragonite suggests rapid cooling of the Upper Trypali Unit during exhumation (*Jolivet et al.*, 1996). However, its lower peak metamorphic temperature may also account for the good preservation of H*P*-L*T* minerals, supporting the hypothesis of nearly isothermal decompression during retrogression and suggesting a similar exhumation process for the entire metamorphic nappe pile (Figure 9a).

In the underlying marble-rich Lower Trypali and Plattenkalk *s.l.* Units, the absence of systematic H*P*-L*T* index mineral hinders accurate *P-T* estimates. However, the presence of highly substituted phengite in the Gigilos beds (Si^{4+} content of 3.28-3.41 apfu; Tables 1, 2) and carpholite in metabauxites (*Seidel et al.*, 1982) within the Plattenkalk *s.l.* Unit support H*P*-L*T* burial conditions for the lowermost part of the nappe stack. More accurate *P-T* estimates from the Kastania phyllites, lateral equivalents of the Gigilos beds in the south Peloponnese, yield 7-8.5 kbar and 310-360 °C (*Blumör et al.*, 1994), consistent with the RSCM temperatures (340-350 °C; Figure 9a).

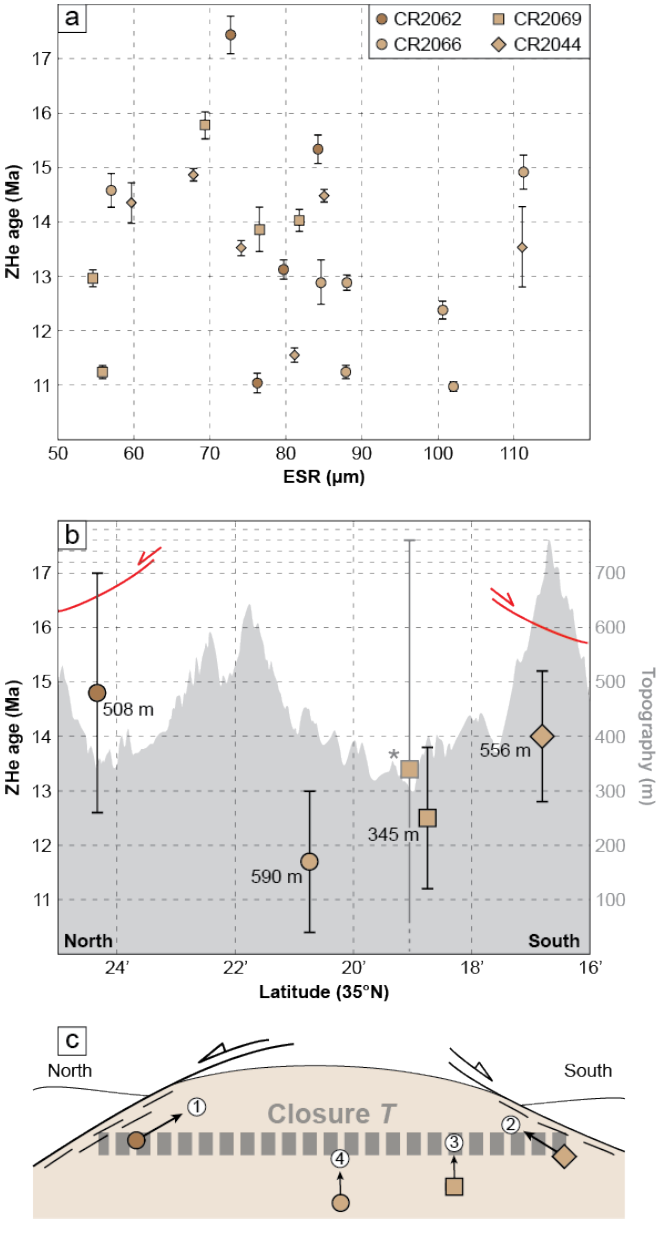

Figure 8 – ZHe ages from the High-*T* and Medium-*T* Phyllite-Quartzite Units. (**a**) Plot of ESR *versus* ZHe age for the full dataset with uncertainties of age data at 2σ. Aliquot #6 of sample CR2069 is not plotted because it yields an anomalously high ZHe age. (**b**) Plot of latitude *versus* ZHe age, showing the N-S distribution of mean ZHe ages. The elevation of dated samples is indicated, along with a N-S topographic profile (in grey). The age with an asterisk (*) represents the ZHe age of sample CR2069 prior to data curation (see Section 8.2). (**c**) Schematic cross-section showing the late-exhumation scenario for the H*P*-L*T* duplex, primarily controlled by the dominant top-to-the-N and top-to-the-S detachments. Dotted line indicates the closure temperature of zircon crystals for (U-Th-Sm)/He thermochronology.

The varying peak-pressure conditions of the tectono-metamorphic nappes highlights a decrease in both maximum temperature and pressure toward the base of the H*P*-L*T* duplex (Figures 9, 10). The maximum-temperature drop between the High-*T* and Medium-*T* Phyllite-Quartzite Units and the Upper Trypali Unit likely reflects a minor decrease in the geothermal gradient along the subduction interface while the nappes were accreted at ~55-60 km depth. However, uncertainties in the maximum pressure, particularly for the Upper Trypali Unit, leave open the possibility that these units were sliced from the subducting lithosphere at progressively shallower depths. Structurally below this, the Plattenkalk *s.l.* Unit was likely detached at lower depths (25-30 km) and recorded a warmer geothermal gradient, consistent with geotherms of the plate interface at crustal depth (Figure 9a). The lithospheric processes responsible for this geothermal gradient increase along the subduction interface will be discussed in Section 8.3 once precise time bounds for this thermal evolution will be established.

8.2 Implication of Rb/Sr and ZHe Ages for Temporal Evolution of the H*P*-L*T* Duplex

The new Rb/Sr and ZHe ages (Figures 6-8; Tables 1, 3), combined with detailed mapping of tectono-metamorphic units, provide new insights into the evolution of the metamorphic nappe stack, from blueschist- and greenschist-facies conditions to shallow crustal levels.

The High-*T* Phyllite-Quartzite Unit yields a moderately reliable Rb/Sr age of 16.4 ± 1.6 Ma (Figure 6a), interpreted as a crystallization age under greenschist-facies conditions as attested by the epidote + chlorite + phengite + paragonite assemblage of the dated sample (Figure 3a; Table 1). The elevated MSWD (= 11) reflecting slight Sr-isotopic disequilibrium among the low-Rb/Sr phases, requires that this age be interpreted with caution. Nevertheless, its consistency with a K/Ar age on white mica from *Seidel et al.* (1982), supports an early Miocene exhumation for this unit (Figures 7a, 11). No precise age is available for the blueschist-facies peak metamorphic conditions (see Supporting Information), setting a minimum timeframe for the basal-accretion event during the late Oligocene-early Miocene.

In the Medium-*T* Phyllite-Quartzite Unit, the 20.8 ± 1.4 Ma Rb/Sr age obtained from a chloritoid-bearing phyllite (sample CR1965b) is interpreted to record near peak-metamorphism conditions of 15-17 kbar and 390-440 °C, as attested by the good alignment of the chloritoid point along

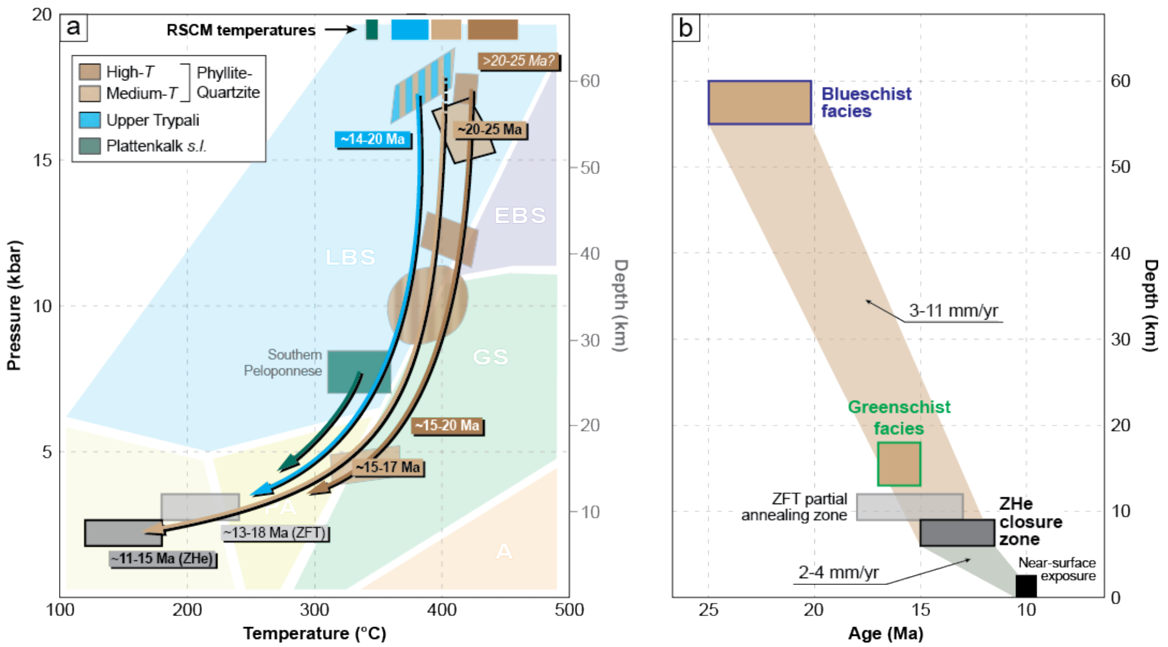

Figure 9 – Metamorphic evolution of the duplex. (**a**) *P*-*T* diagram compiling the stability fields from H*P*-L*T* units with interpreted exhumation paths, as well as the geochronological and thermochronological constraints. RSCM temperatures are from *Menant et al.* (2026) (this issue). Ages from this study are shown in bold. Zircon fission-track (ZFT) ages are from *Thomson et al.* (1998) and *Marsellos et al.* (2010). (**b**) Age-depth diagram illustrating the exhumation rates inferred for the Medium-*T* Phyllite-Quartzite Unit.

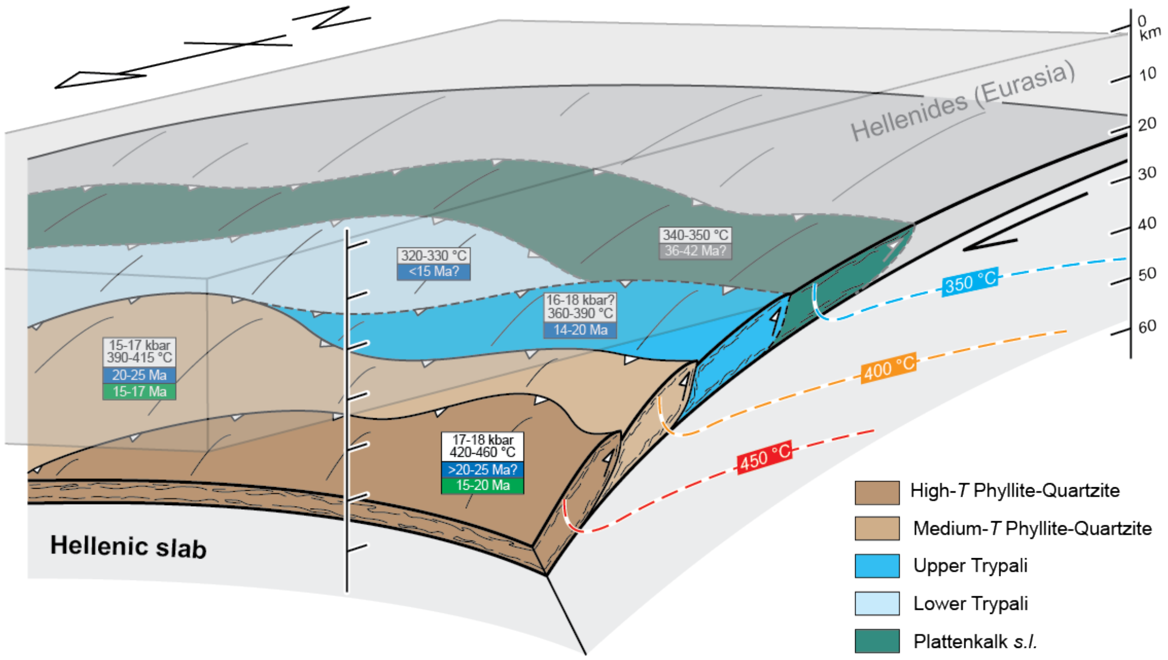

Figure 10 – Schematic view of the Hellenic subduction zone showing the succession of detachment of tectonic slices during the late Oligocene-middle Miocene that later formed the H*P*-L*T* duplex in western Crete. *P*-*T*-*t* constraints are reported for each unit. In blue: basal-accretion-related blueschist-facies ages. In green: exhumation-related greenschist-facies ages.

the regression line (Figures 3b, 6c). This age displays an acceptable MSWD (= 4.1) reflecting minor scatter among white-micas Rb/Sr isotopic data due to diffusion, deformation or fluid-rock interaction processes (*Smye et al.*, 2021; *Glodny and Ring*, 2022), supporting its geological significance. A slightly older Rb/Sr age of 24.3 ± 1.2 Ma from the same units should be considered with caution because of its slightly high MSWD (= 8.1) (Figure 6b). Nevertheless, when combined with existing geochronological constraints (*Seidel et al.*, 1982; *Jolivet et al.*, 1996), these ages support a protracted blueschist-facies event between 25 and 20 Ma, likely corresponding to peak-pressure conditions during detachment of the Medium-*T* Phyllite-Quartzite Unit from the subducting crust (Figures 7a, 11). Consistently, recent K/Ar ages of 21-26 Ma on illite/white-mica mixtures from fault gouges (*Ring et al.*, 2022) suggests that these structures were active at H*P*-L*T* conditions, although they should not be considered as major tectonic contacts (see

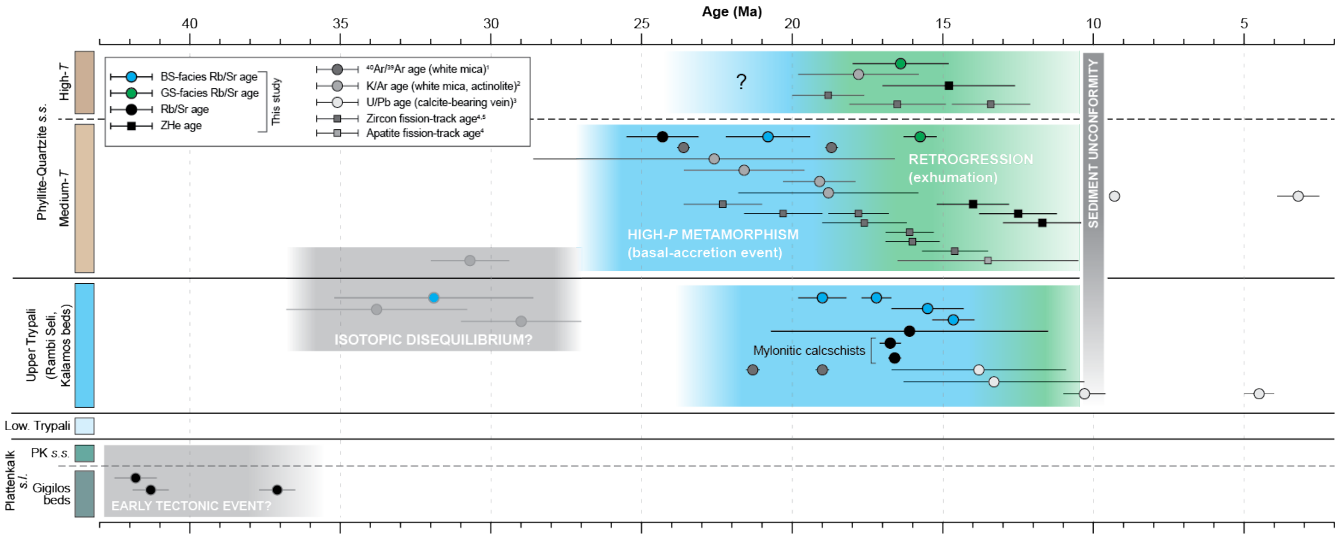

Figure 11 – Compilation of geochronological and thermochronological ages, along with their associated standard deviations, for the H*P*-L*T* duplex in western Crete. BS: Blueschist. GS: Greenschist. PK: Plattenkalk. (1) *Jolivet et al.* (1996); (2) *Seidel et al.* (1982); (3) *Ring et al.* (2022); (4) *Thomson et al.* (1998); (5) *Marsellos et al.* (2010).

discussion *Menant et al.*, 2026, this issue). Subsequent retrogression occurred during the middle Miocene, as recorded by the 15.75 ± 0.55 Ma Rb/Sr age obtained from a top-to-the-NNE greenschist-facies shear zone located in the vicinity of the underlying Upper Trypali Unit (Figures 2c, 6d). Despite a high MSWD (= 40) attributed to Sr-isotopic disequilibrium among the low-Rb/Sr phases, this age provides evidence that this major tectonic contact, formed during the H*P*-L*T* nappe stacking, was reworked as an extensional shear zone during duplex exhumation.

The underlying Upper Trypali Unit yields consistent Rb/Sr ages between 14 and 20 Ma obtained from lawsonite-bearing phyllite and lawsonite- and carpholite-bearing veins (Figure 6e, h-j). Low MSWD values obtained for part of the dataset support the geological significance of these ages that are interpreted to record crystallization under blueschist-facies conditions. Combined with consistent ^{40}Ar/^{39}Ar ages on white mica (*Jolivet et al.*, 1996) and U/Pb dating on calcite from a lawsonite- and aragonite-bearing vein (*Ring et al.*, 2022), these results support an early-middle Miocene deep slicing event along the subduction interface, partly overlapping the exhumation stage of the Medium-*T* Phyllite-Quartzite Unit (Figure 11). Similar Rb/Sr ages of ~16-17 Ma, displaying low to moderately elevated MSWD, were recorded in mylonitic calcschists exposed (i) in the footwall of the partly reworked thrust contact between the Upper Trypali and the Medium-*T* Phyllite-Quartzite Units and (ii) in the footwall of the detachment between the Upper Trypali and the Gavrovo-Tripolitza Units (Figures 2e, 6f-g, 7b). These Rb/Sr ages display relatively low MSWD and are confidently interpreted to date the late stages of mylonitic deformation along these two structures that were synchronously active under H*P*-L*T* conditions when the Upper Trypali Unit was inserted into the nappe stack.

A surprisingly old Rb/Sr age of 41.79 ± 0.66 Ma from the Gigilos beds (Figures 6l, 7a-b, 11), supported by a second, less robust age (sample CR1955a; see Supporting Information), is the first obtained for the Plattenkalk *s.l.* Unit. The high MSWD (= 21) requires that this age be interpreted with caution, but it may nevertheless indicate that an early tectono-metamorphic event is preserved in this siliciclastic formation. While no isotopic disequilibrium appears from the isochron (Figure 6l), partial inheritance cannot be ruled out, as shown by zoned calcite and variable phengite composition in the two analyzed samples (Figures 3e, 4d, see also Supporting Information). The low RSCM temperatures of this unit (~340-350 °C) (*Menant et al.*, 2026, this issue) support a possible incomplete isotopic reequilibration during the burial and exhumation of the Plattenkalk *s.l.* Unit, similar to the Phyllite-Quartzite *s.l.* Unit in eastern Crete that preserves isotopic inheritance (*Jolivet et al.*, 1996; *Brix et al.*, 2002).

Several samples from the High-*T* and Medium-*T* Phyllite-Quartzite Units and the Upper Trypali Unit show significant isotopic disequilibrium, yielding geologically meaningless Rb/Sr ages between 31.9 ± 3.3 Ma and 63 ± 21 Ma (Figure 10). This disequilibrium, likely due to inherited isotopic signatures, is indicated by distinct Sr isotopic compositions within the mica populations and disequilibrium textures (see Supporting Information). These questionable ages overlap with some K/Ar ages on white micas (Seidel *et al.*, 1982) and a K/Ar age cluster of 37-40 Ma from fault gouges (Ring *et al.*, 2022) that are consistently interpreted as mixing ages.

The late cooling event is well constrained by ZHe ages, except for sample CR2069 that displays an over-dispersed age population and a poorly constrained mean age of 13.4 ± 4.2 Ma (Figures 7c, 8, Table 3). For this sample, aliquot #6 yields an anomalously old age (23.2 ± 0.8 Ma), comparable to the nearby Rb/Sr age of sample CR1925a (24.3 ± 1.2 Ma; Figure 7), which cannot be explained by differences in closure temperature caused by radiation damage or grain size (Figure 8a); it is therefore excluded from further interpretation. Then, omitting either aliquot #3 (oldest) or #5 (youngest) removes the over-dispersion and yields mean ages of 12.5 ± 1.3 Ma and 14.0 ± 1.2 Ma, respectively. Again, because the age pattern does not reflect varying closure temperature (Figure 8a), other factors, such as crystal zoning, are likely responsible for the anomalous ages, justifying the exclusion of one of these aliquots. Given the structural position of sample CR2069 within the nappe stack, we favor the younger age interpretation as the most plausible, which does not modify the overall ~12-15 Ma cooling age range for the High-*T* and Medium-*T* Phyllite-Quartzite Units.

The oldest ages, localized in the footwall of the two detachments bounding the H*P*-L*T* duplex in the north and south, overlap the Rb/Sr ages, indicating a fast exhumation mostly controlled by these low-angle extensional structures. A consistent decrease of ZHe ages toward the center of the nappe stack suggests an almost symmetrical late exhumation stage, although the slightly older ZHe age in the footwall of the top-to-the-N detachment may indicate its predominance (Figure 8c). These ZHe ages align with zircon and apatite fission-track ages that are generally slightly older (Figures 7c, 10) (*Thomson et al.*, 1998; *Marsellos et al.*, 2010). However, only the <18-Ma zircon fission-track ages overlap the greenschist-facies overprint at $T \leq 360$ °C (Figure 9a) (*Jolivet et al.*, 1996), suggesting older fission-track ages may be overestimated. The duplex's surface exposure is constrained at ~10 Ma, based on the oldest sediments unconformably deposited on the metamorphic nappe stack (*van Hinsbergen and Meulenkamp*, 2006). This final exhumation phase is associated with late tectonic and fluid pulses, partly coeval with calcite-bearing veins associated with N-S striking faults cutting the duplex and dated to the late Miocene-Pliocene (*Ring et al.*, 2022).

Combining geochronological and thermochronological data, early exhumation rates are estimated at 3-11 mm/yr for the Medium-*T* Phyllite-Quartzite Unit (Figure 9b), consistent with the ≥4 mm/yr exhumation rates proposed by *Thomson et al.* (1998). A significant reduction in exhumation rates to 2-4 mm/yr is calculated for the subsequent exhumation in the shallow forearc crust (i.e., <10 km depth) in the late Miocene. This slowdown likely resulted from the cessation of the top-to-the-N Cretan detachment activity, which had been more efficient in exhuming the duplex than the high-angle normal faults that later cut it, thereby reducing the efficiency of tectonic unroofing.

8.3 Implications for the Late Cenozoic Evolution of the Hellenic Subduction

Our field observations, P-T estimates and geochronological and low-*T* thermochronological data from the paleo-accretionary duplex in western Crete allow us to propose a detailed scenario for the evolution of the Hellenic subduction zone in the late Cenozoic, as illustrated by scaled lithospheric cross-sections (Figure 12). In the late Eocene, the subduction of the partly oceanic Pindos basin ended and the Gavrovo-Tripolitza carbonate platform started to be frontally accreted to the Hellenic margin, as attested by the late Eocene-early Oligocene age of its flysch cover (*Aubouin*, 1959). At this time, the metavolcanic and metasedimentary protoliths of the Phyllite-Quartzite *s.l.* Unit and Plattenkalk *s.l.* Unit were located 100-400 km south of the subduction zone (Figure 12a). A late Eocene tectono-metamorphic event may have affected the Ionian platform (i.e., the protolith of the Plattenkalk *s.l.* Unit), potentially representing a far-field expression of the accretion of the thick Gavrovo-Tripolitza platform at the deformation front. However, further investigations are needed to confirm this hypothesis, as these unexpectedly old Rb/Sr ages may also reflect partial isotopic inheritance (see Section 8.2).

During the Oligocene to early Miocene, the Hellenic subduction propagated southward, triggering back-arc basin opening and the exhumation of metamorphic core complexes in the Cyclades (*Lister et al.*, 1984; *Jolivet and Brun*, 2010). Further south, subduction of clastic and volcano-sedimentary layers below the frontally accreting Gavrovo-Tripolitza and Ionian domains led to the formation of the High-*T* and Medium-*T* Phyllite-Quartzite Units under blueschist-facies conditions (Figure 12b) (*Seidel et al.*, 1982; *Jolivet et al.*, 1996). By ~20-25 Ma, these units were successively detached from the downgoing slab at ~55-60-km depth (Figure 10). This was followed by a third slicing event at a similar (or slightly shallower) depth, resulting in the formation of the Upper Trypali Unit at ~15-20 Ma. These units experienced fast and asymmetric exhumation from mantle to crustal depth (≥3 mm/yr; Figure 9b), likely as part of an extrusion wedge above the subduction interface, marked by the coeval activity of (i) mylonitic shear zones bounding the units and (ii) the top-to-the-N Cretan detachment at the top of the metamorphic duplex (Figures 2e, 6f-g, 12b) (*Jolivet et al.*, 1996; *Grasemann et al.*, 2019; *Menant et al.*, 2026). A similar mechanism has been already proposed for the Phyllite-Quartzite *s.l.* Unit in Peloponnese (*Xypolias and Koukouvelas*, 2001; *Jolivet et al.*, 2010; *Wicker and Bufféral*, 2024), as well as for the syn-orogenic exhumation stage of the Cycladic Blueschist Unit that took place further north in the Eocene (*Jolivet and Brun*, 2010; *Ring and Glodny*, 2010).

In the early middle Miocene, the High-*T* and Medium-*T* Phyllite-Quartzite Units reached mid-forearc crustal levels (~14-18 km), where they were affected by N-S-directed, bivergent ductile shear zones under greenschist-facies conditions (Figures 2c, 9). Coevally, the Upper Trypali Unit was finished its early exhumation as an extruded slice under blueschist-facies conditions (Figure 12c). At this point, the lower Trypali and the Plattenkalk *s.l.* Units were successively underthrust at ~25-30 km depth, as attested by their lower RSCM temperatures and peak-pressure estimates

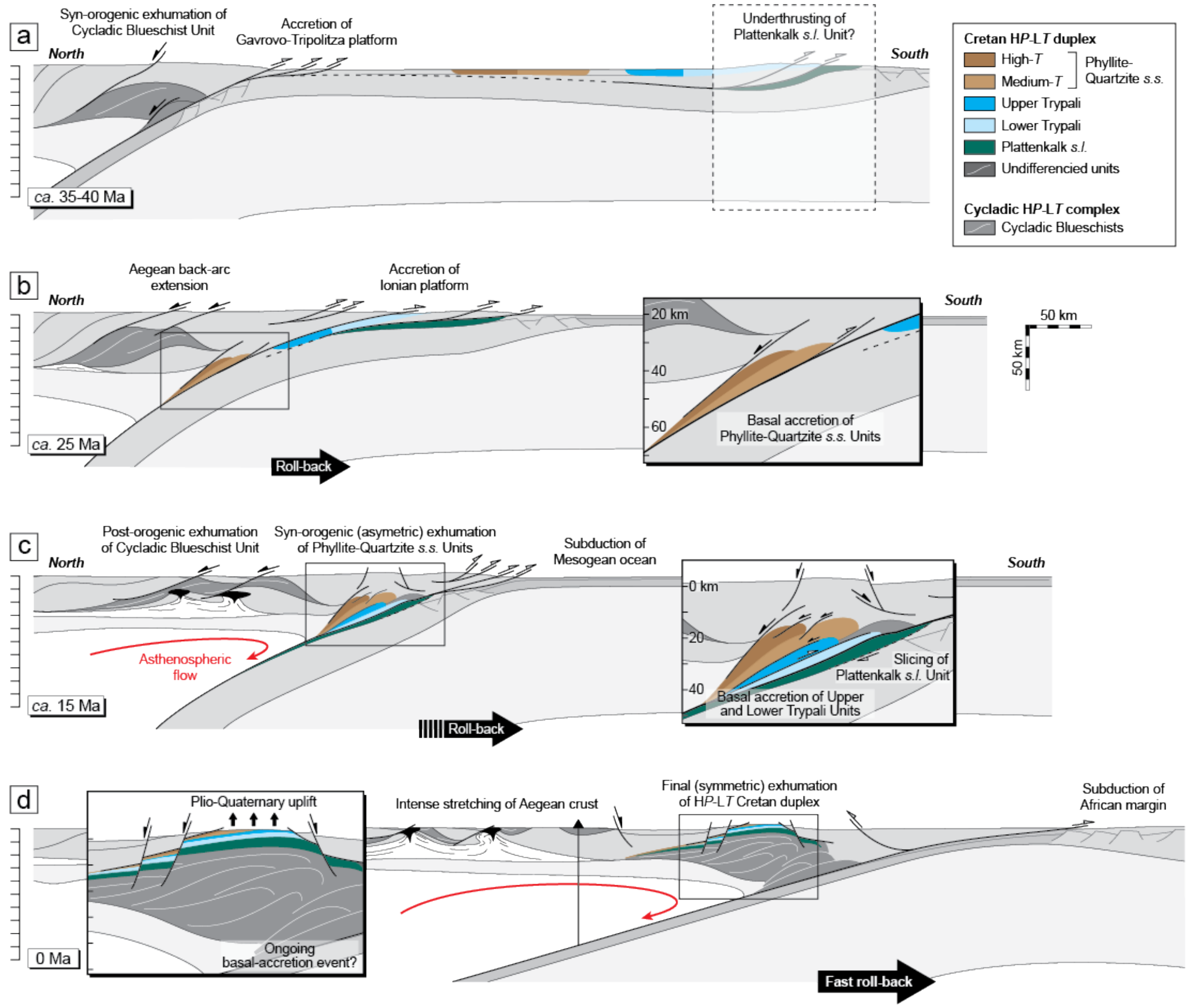

Figure 12 – a-d) Lithospheric-scale cross-sections illustrating the temporal evolution of the Hellenic subduction zone since the late Eocene, with successive burial, basal-accretion and exhumation stages of the H*P*-L*T* units that constitute the paleo-accretionary complex of western Crete. The cross-sections, drawn to scale using the kinematic reconstructions of *Menant et al.* (2016a), have been modified from *Bouhot et al.* (2025).

(Figures 9a, 11c) (*Blumör et al.*, 1994; *Menant et al.*, 2026). This different accretion depth is associated with an increase in the apparent thermal gradient, a pattern also noted for the Phyllite-Quartzite *s.l.* Unit in southern Peloponnese (*Bouhot et al.*, 2025), which may reflect progressively warmer conditions near the subduction interface through time. This trend contrasts with the largely invariant thermal regime proposed for continental subduction by Agard and Vitale-Brovarone (2013), based on a *P-T-t* compilation of H*P*-L*T* terranes exhumed during continental subduction. In the Hellenic subduction zone, the increasing geothermal gradient may reflect enhanced asthenospheric flux into the mantle wedge driven by accelerated slab roll-back following major slab tearing beneath western Anatolia at ~15 Ma (*Dilek and Altunkaynak*, 2009; *Jolivet et al.*, 2013; *Menant et al.*, 2016b).

These five basal-accretion events contributed to the growth of a thick H*P*-L*T* duplex beneath the Hellenic forearc domain, stretching from eastern Crete to northern Peloponnese (*Seidel et al.*, 1982; *Jolivet et al.*, 2010). Exhumation from lower to upper crustal depths occurred in the middle-late Miocene at slower rates (2-4 mm/yr; Figure 9b). This almost symmetrical late exhumation stage was accommodated by N-S extension, primarily along major ductile-brittle detachments, including the top-to-the-N Cretan detachment (Figures 11, 12c) (*Fassoulas et al.*, 1994; *Jolivet et al.*, 1996; *Papanikolaou and Vassilakis*, 2010; *Grasemann et al.*, 2019; *Ring et al.*, 2022; *Menant et al.*, 2026). During this period, syn-tectonic half-graben basins formed, filled with conglomerates containing clasts of the non-metamorphic Gavrovo-Tripolitza and Pindos Units (*van Hinsbergen and Meulenkamp*, 2006; *Seidel et al.*, 2007; *Zachariasse and van Hinsbergen*, 2025). It is also during this period that a E-W-directed, trench-parallel extension developed in response to the progressive bending of the subduction zone during its fast retreat (*van Hinsbergen and Meulenkamp*, 2006; *Marsellos et al.*, 2010). Switches between trench-perpendicular and trench-parallel extension likely occurred during the protracted retreat and curvature of the Hellenic slab, leading to the exhumation of the entire duplex of western Crete as a dome into the forearc upper crust. This late exhumation stage occurred during the middle Miocene in eastern Crete (*Grasemann et al.*, 2019) and during the late Miocene in Peloponnese and Kythira (*Marsellos et al.*, 2010; *Wicker*, 2023). This diachronic exhumation likely resulted from variations in trench-parallel stretching of the Hellenic forearc crust caused by differential slab retreat (*Jolivet et al.*, 2010; *Marsellos et al.*, 2010; *van Hinsbergen and Schmid*, 2012; *Menant et al.*, 2016a). The final exhumation of the HP-LT nappe stack in the late Miocene was accommodated by N-S and E-W-striking, high-angle normal faults that also led to the opening of the Cretan Sea (Figure 12d) (*Angelier et al.*, 1982; *Zachariasse et al.*, 2011; *Nicol et al.*, 2020). Fault-bounded basins with metamorphic-clast bearing sedimentary layers were then emplaced, marking the surface exposure of the duplex at ~10 Ma in Crete (*Meulenkamp et al.*, 1994; *van Hinsbergen and Meulenkamp*, 2006).

8.4 Timescale Assessment for Accretion-controlled Uplift and Forearc Deformation

The new tectonic, petrological and geochronological constraints reported in these two companion papers (*Menant et al.*, 2026, this issue; this study) provide key insights on the dynamics of basal-accretion process suspected along many active subduction zones worldwide (*Scholl*, 2021; *Angiboust et al.*, 2022). In western Crete, the five tectono-metamorphic units yield contrasted P-T(-t) evolutions witnessing a succession of slicing episodes along the plate interface at depths ranging from 25-30 km to 55-60 km (Figures 9, 12). Subsequent decollement and imbrication of cover units into an antiformal stack have also been reported from other HP-LT paleo-accretionary wedges formed during continental subduction (*Agard and Vitale-Brovarone*, 2013). According to these authors, decreasing peak metamorphic conditions toward the base of the nappe stack, as observed in western Crete (Figure 10) or in Cuba (*García-Casco et al.*, 2008), may reflect stronger mechanical coupling at the base of the upper continental plate, promoting successive slicing events within the sedimentary cover of the subducting plate.

Although the timing of peak metamorphism and the subsequent exhumation stage were not constrained for all units in western Crete, two slicing episodes between ~26 Ma and ~15 Ma are recognized, resulting in the formation of the Medium-T Phyllite-Quartzite and Upper Trypali Units (Figure 10). By extension, and considering ZHe late cooling ages of 12-15 Ma (Figure 8), three additional accretion events likely occurred in a time span ranging from the late Oligocene to the middle Miocene, leading to the formation of the High-T Phyllite-Quartzite, the Lower Trypali and the Plattenkalk *s.l.* Units. Altogether, these time constraints suggest a recurrence time for basal accretion events along this segment of the Hellenic subduction zone of ~2-3 Myr. A similar trend of down-stepping metamorphic ages was reported from other paleo-accretionary duplexes worldwide, supporting this Myr-scale cadence of deep slicing events; e.g., the Cyclades (*Laurent et al.*, 2021; *Glodny and Ring*, 2022), western Alps (*Angiboust et al.*, 2014; *Bonnet et al.*, 2022), Alpine Corsica (*Vitale Brovarone and Herwartz*, 2013), Franciscan complex (*Wakabayashi*, 2015) and Zagros suture zone (*Angiboust et al.*, 2016).

One consequence of the succession of large mass-flux events at depth in subduction zones is the pulsed growth of high forearc topography, typically located near the coastline, as predicted by both analog and numerical models (*Lohrmann et al.*, 2006; *Menant et al.*, 2020). Recently, Myr-scale, accretion-controlled periodic uplift stages have been documented along the Peruvian subduction zone through the study of uplifted paleo-shorelines (*Regard et al.*, 2021). Interestingly, sedimentary records from now-exposed forearc basins in Crete and investigations on marine terrasses in the neighboring Karpathos island reveal a Myr-scale succession of subsidence then uplift during the late Miocene and the Plio-Quaternary, respectively (*Meulenkamp et al.*, 1994; *van Hinsbergen and Meulenkamp*, 2006). This recent, Myr-long uplift event may have been controlled by one or several deep-accretion episodes along the Hellenic subduction zone (*Gallen et al.*, 2014). The collision of the African plate with the tip of the Mediterranean ridge (i.e., the present-day accretionary wedge) has also been proposed as a mechanism to explain the emergence of Crete during the Pliocene (*van Hinsbergen and Meulenkamp*, 2006). However, this hypothesis would predict a deceleration in the retreat of Crete that is not supported by GPS data showing a relatively consistent and rapid southwestward migration of the entire Hellenic forearc (*Nocquet*, 2012). Conversely, a deeper origin for the episodic growth and emergence of Crete, likely driven by past and ongoing basal-accretion events, appears to be a more plausible mechanism (Figure 12d).

Given the forearc topographic response, basal-accretion events along the plate interface are likely to influence the stress state and, consequently, the deformation history of the forearc crust. Investigating the deformation fabrics recorded in the HP-LT metamorphic duplex of western Crete thus provide valuable insights into the tectonic evolution of the Hellenic forearc domain over at least the past 25 Myr; i.e., from the earliest basal-accretion event to the present day. The widespread occurrence of N-S trending lineation, stretched boudins and extensional shear zones in blueschist- and greenschist-facies rocks, along with major ductile-brittle detachments and high-angle normal faults, is consistent with a dominant extensional regime during the exhumation of metamorphic nappe stack (*Fassoulas et al.*, 1994; *Jolivet et al.*, 1994; *van Hinsbergen and Meulenkamp*, 2006; *Marsellos et al.*, 2010; *Nicol et al.*, 2020). In contrast, the recognition of ductile and brittle structures indicative of compressional to transpressional deformation, without a clear temporal relationship to the extensional fabrics, suggests changes in the stress regime over a timescale that remains poorly constrained (*Tortorici et al.*, 2010; *Chatzaras et al.*, 2013; see also discussion in Menant *Menant et al.*, 2026, this issue). By analogy with observations from megathrust and forearc earthquakes, which demonstrate that major seismic ruptures can transiently modify the forearc stress state (*Wang et al.*, 2019) and trigger reverse seismic or aseimic slip on fault segments (*Shirzaei et al.*, 2012; *Mouslopoulou et al.*, 2020), episodic basal-accretion events might have contributed to Myr-scale stress perturbations in the forearc crust. These perturbations could plausibly result in composite deformation patterns reflecting the cumulative effects of such events. This hypothesis is broadly consistent with natural observations and analog modeling that highlight the influence of mass fluxes on the mechanical stability of convergent margins (*Lallemand et al.*, 1994). However, further research is required to test this hypothesis, particularly through precise geochronological dating of the varied structural fabrics and numerical investigation on the forearc's tectonic response to deep accretionary events.

9 Conclusion

This study provides a comprehensive reconstruction of the contrasted *P*-*T*-*t* evolution of the five tectono-metamorphic units that compose the H*P*-L*T* paleo-accretionary duplex of western Crete in order to unravel the dynamics of deep accretion and exhumation along the Hellenic forearc margin during the Oligocene-Miocene. By integrating new petrological observations, thermodynamic modeling and geochronological and thermochronological data, we thus report for the first time a decrease in the *P*-*T* peak conditions and the Rb/Sr ages of the blueschist- and greenschist-facies ages from the top to the base of the duplex. One possible exception might be interpreted from the old ~41-42-Ma ages in the Plattenkalk *s.l.* Unit that witness either an inherited isotopic signature or an earlier tectonic event. Apart from these questionable ages, peak-metamorphic-condition ages, ranging from >25 Ma to ~14 Ma, are interpreted as the timing of the successive deep slicing events along the subduction interface. The exhumation stage mainly occurred in the Middle Miocene, with rates initially fast (3-11 mm/yr) and then slower (2-4 mm/yr), leading to the surface exposure of the nappe stack by the late Miocene. These rapid accretion and exhumation processes enabled the formation of a 10s-km-thick H*P*-L*T* duplex, driven by the coeval fast southward retreat of the Hellenic subduction zone enhanced by slab tearing from ~15 Ma.

This work further suggests a recurrence time of ~2-3-Myr for basal-accretion events along this segment of the Hellenic subduction, occurring between 20 and 60 km depth during the late Oligocene to middle Miocene. This Myr-scale cadence of deep slicing events, observed in other H*P*-L*T* paleo-duplexes worldwide, indicates that such processes could provide a characteristic timescale for accretion-related surface uplift and forearc deformation. This topographic and tectonic signature may be detectable at active forearc margins and therefore merit closer attention in future studies to track deep, and often overlooked, mass-flux events. In light of this, the evidence supports the ongoing occurrence of basal-accretion events beneath Crete from the late Oligocene to the present, likely contributing to the island's emergence.

Acknowledgements

This work was funded by the A. von Humboldt foundation via a postdoctoral fellowship. The field campaigns carried on during this study were authorized by the Hellenic Survey of Geology and Mineral Exploration (HSGME) via the delivery of the work permit No. 3691/13-8-20. Nicolai Klitscher is warmly thanked for producing the thin sections and Franziska Wilke and Jesus Muñoz-Montecinos are sincerely appreciated for their assistance with the acquisition of electron probe microanalysis data. The use of the scanning electron microprobe in the "Potsdam Imaging and Spectral Analysis Facility" (PISA) is gratefully acknowledged. We thank Graeme Eagles for his editorial handling of the manuscript and two anonymous reviewers for their thoughtful comments.

Author contributions

AM: conceptualization of the study, project funding, field work, original draft writing. **JG**: providing guidance and contributed to sample preparation and Rb/Sr analyses. **SA**: conceptualization of the study, field work, providing assistance with thermodynamic modeling. **ERS**: carrying out (U-Th-Sm)/He analyses. **EB**, **LJ**: field work. **OO**: conceptualization of the study. All the authors contributed to data analysis, as well as the review and editing of the original draft.

Data availability

The list of analyzed samples, including their GPS coordinates and elevation, and the complete Rb/Sr dataset are provided in Supporting Information.

Competing interests

The authors declare no competing interests.

Peer review

This publication was peer-reviewed by two anonymous reviewers. The full peer-review report can be found here: Review Report.

Copyright notice

References

Agard, P., and A. Vitale-Brovarone (2013), Thermal regime of continental subduction: The record from exhumed HP–LT terranes (New Caledonia, Oman, Corsica), *Tectonophysics*, *601*, 206–215, https://doi.org/10.1016/j.tecto.2013.05.011.

Angelier, J., N. Lybéris, X. Le Pichon, E. Barrier, and P. Huchon (1982), The tectonic development of the hellenic arc and the sea of crete: A synthesis, *Tectonophysics*, *86*(1-3), 159–196, https://doi.org/10.1016/0040-1951(82)90066-x.

Angiboust, S., J. Glodny, O. Oncken, and C. Chopin (2014), In search of transient subduction interfaces in the Dent Blanche–Sesia Tectonic System (W. Alps), *Lithos*, *205*, 298–321, https://doi.org/10.1016/j.lithos.2014.07.001.

Angiboust, S., P. Agard, J. Glodny, J. Omrani, and O. Oncken (2016), Zagros blueschists: Episodic underplating and long-lived cooling of a subduction zone, *Earth and Planetary Science Letters*, *443*, 48–58, https://doi.org/10.1016/j.epsl.2016.03.017.

Angiboust, S., A. Menant, T. Gerya, and O. Oncken (2022), The rise and demise of deep accretionary wedges: A long-term field and numerical modeling perspective, *Geosphere*, *18*(1), 69–103, https://doi.org/10.1130/ges02392.1.

Aubouin, J. (1959), Contribution à l'étude de la Grèce septentrionale; les confins de l'Epire et de la Thessalie, *Ann. Geol. Pays Hellen.*, *10*, 1–483.

Blumör, T., J. Dollinger, M. Knobel, M. Mutter, A. Zarda, and G. Kowalczyk (1994), Plattenkalk series and Kastania phyllites of the Taygetos Mts.: new results on structure and succession, *Deltio tis Ellinikis Geologikis Etairias/Bulletin of the Geological Society of Greece*, *30*(2), 83–92.

Bonnet, G., C. Chopin, M. Locatelli, A. R. C. Kylander-Clark, and B. R. Hacker (2022), Protracted subduction of the European hyperextended margin revealed by rutile U-Pb geochronology across the Dora-Maira massif (western alps), *Tectonics*, *41*(4), e2021TC007,170, https://doi.org/10.1029/2021tc007170.

Bouhot, M., A. Menant, C. Ganino, S. Angiboust, O. Oncken, L. Jolivet, D. Deldicque, N. Skarpelis, and F. Orange (2025), 3D Petro-structural evolution of the high pressure-low temperature Phyllite-Quartzite nappe pile in southern Peloponnese, Greece, *Tectonics*, *44*(12), e2025TC009,089, https://doi.org/10.1029/2025tc009089.

Brix, M. R., B. Stöckhert, E. Seidel, T. Theye, S. N. Thomson, and M. Küster (2002), Thermobarometric data from a fossil zircon partial annealing zone in high pressure–low temperature rocks of eastern and central Crete, Greece, *Tectonophysics*, *349*(1-4), 309–326, https://doi.org/10.1016/s0040-1951(02)00059-8.

Chatzaras, V., P. Xypolias, S. Kokkalas, and I. Koukouvelas (2013), Tectonic evolution of a crustal-scale oblique ramp, Hellenides thrust belt, Greece, *Journal of Structural Geology*, *57*, 16–37, https://doi.org/10.1016/j.jsg.2013.10.003.

Clift, P., and P. Vannucchi (2004), Controls on tectonic accretion versus erosion in subduction zones: Implications for the origin and recycling of the continental crust: SUBDUCTION TECTONICS, *Reviews of Geophysics (Washington, D.C.: 1985)*, *42*(2), https://doi.org/10.1029/2003rg000127.

Connolly, J. A. D. (2005), Computation of phase equilibria by linear programming: A tool for geodynamic modeling and its application to subduction zone decarbonation, *Earth and Planetary Science Letters*, *236*(1-2), 524–541, https://doi.org/10.1016/j.epsl.2005.04.033.

Creutzburg, N., and E. Seidel (1975), zum stand der Geologie des präneagens auf Kreta, *N. Jb. Geol. Paläont. Abh.*, *149*(3), 363–383.

Dilek, Y., and S. Altunkaynak (2009), Geochemical and temporal evolution of Cenozoic magmatism in western Turkey: mantle response to collision, slab break-off, and lithospheric tearing in an orogenic belt, *Geological Society Special Publication*, *311*(1), 213–233, https://doi.org/10.1144/sp311.8.

Fassoulas, C., A. Kilias, and D. Mountrakis (1994), Postnappe stacking extension and exhumation of high-pressure/low-temperature rocks in the island of Crete, Greece, *Tectonics*, *13*(1), 127–138, https://doi.org/10.1029/93tc01955.

Flowers, R. M., R. A. Ketcham, E. Enkelmann, C. Gautheron, P. W. Reiners, J. R. Metcalf, M. Danišík, D. F. Stockli, and R. W. Brown (2023), (U-Th)/He chronology: Part 2. Considerations for evaluating, integrating, and interpreting conventional individual aliquot data, *Geological Society of America Bulletin*, *135*(1-2), 137–161, https://doi.org/10.1130/b36268.1.

Fuhrman, M., and D. Lindsley (1988), Ternary-feldspar modeling and thermometry, *The American Mineralogist*, *73*(3-4), 201–215.

Galetto, A., V. Georgieva, V. H. García, M. Zattin, E. R. Sobel, J. Glodny, S. Bordese, G. Arzadún, F. Bechis, A. T. Caselli, and R. Becchio (2021), Cretaceous and Eocene rapid cooling phases in the Southern Andes (36°–37°S): Insights from low-temperature thermochronology, U-Pb geochronology, and inverse thermal modeling from Domuyo area, Argentina, *Tectonics*, *40*(6), https://doi.org/10.1029/2020tc006415.

Gallen, S. F., K. W. Wegmann, D. R. Bohnenstiehl, F. J. Pazzaglia, M. T. Brandon, and C. Fassoulas (2014), Active simultaneous uplift and margin-normal extension in a forearc high, Crete, Greece, *Earth and Planetary Science Letters*, *398*, 11–24, https://doi.org/10.1016/j.epsl.2014.04.038.

García-Casco, A., M. A. Iturralde-Vinent, and J. Pindell (2008), Latest cretaceous collision/accretion between the Caribbean plate and caribeana: Origin of metamorphic terranes in the greater Antilles, *International Geology Review*, *50*(9), 781–809, https://doi.org/10.2747/0020-6814.50.9.781.

Glodny, J., and U. Ring (2022), The Cycladic Blueschist Unit of the Hellenic subduction orogen: Protracted high-pressure metamorphism, decompression and reimbrication of a diachronous nappe stack, *Earth-Science Reviews*, *224*(103883), 103,883, https://doi.org/10.1016/j.earscirev.2021.103883.

Glodny, J., U. Ring, and A. Kühn (2008), Coeval high-pressure metamorphism, thrusting, strike-slip, and extensional shearing in the Tauern Window, Eastern Alps: TAUERN WINDOW EVOLUTION, *Tectonics*, *27*(4), https://doi.org/10.1029/2007tc002193.

Grasemann, B., D. A. Schneider, and A. Rogowitz (2019), Back to normal: Direct evidence of the Cretan Detachment as a north-directed normal fault during the Miocene, *Tectonics*, *38*(8), 3052–3069, https://doi.org/10.1029/2019tc005582.

Guenthner, W. R., P. W. Reiners, R. A. Ketcham, L. Nasdala, and G. Giester (2013), Helium diffusion in natural zircon: Radiation damage, anisotropy, and the interpretation of zircon (U-Th)/He thermochronology, *American Journal of Science*, *313*(3), 145–198, https://doi.org/10.2475/03.2013.01.

Gutscher, M.-A., N. Kukowski, J. Malavieille, and S. Lallemand (1996), Cyclical behavior of thrust wedges: Insights from high basal friction sandbox experiments, *Geology*, *24*(2), 135, https://doi.org/10.1130/0091-7613(1996)024<0135:cbotwi>2.3.co;2.

He, J. J. Y., and P. W. Reiners (2022), A revised alpha-ejection correction calculation for (U–Th) / He thermochronology dates of broken apatite crystals, *Geochronology*, *4*(2), 629–640, https://doi.org/10.5194/gchron-4-629-2022.

Holland, T. J. B., and R. Powell (2011), An improved and extended internally consistent thermodynamic dataset for phases of petrological interest, involving a new equation of state for solids: THERMODYNAMIC DATASET FOR PHASES OF PETROLOGICAL INTEREST, *Journal of Metamorphic Geology*, *29*(3), 333–383, https://doi.org/10.1111/j.1525-1314.2010.00923.x.

Jolivet, L., and J.-P. Brun (2010), Cenozoic geodynamic evolution of the Aegean, *International Journal of Earth Sciences*, *99*(1), 109–138, https://doi.org/10.1007/s00531-008-0366-4.

Jolivet, L., J. M. Daniel, C. Truffert, and B. Goffé (1994), Exhumation of deep crustal metamorphic rocks and crustal extension in arc and back-arc regions, *Lithos*, *33*(1-3), 3–30, https://doi.org/10.1016/0024-4937(94)90051-5.

Jolivet, L., B. Goffé, P. Monié, C. Truffert-Luxey, M. Patriat, and M. Bonneau (1996), Miocene detachment in Crete and exhumation P-T-t paths of high-pressure metamorphic rocks, *Tectonics*, *15*(6), 1129–1153, https://doi.org/10.1029/96tc01417.

Jolivet, L., F. Trotet, P. Monié, O. Vidal, B. Goffé, L. Labrousse, P. Agard, and B. Ghorbal (2010), Along-strike variations of P–T conditions in accretionary wedges and syn-orogenic extension, the HP–LT Phyllite–Quartzite Nappe in Crete and the Peloponnese, *Tectonophysics*, *480*(1-4), 133–148, https://doi.org/10.1016/j.tecto.2009.10.002.

Jolivet, L., C. Faccenna, B. Huet, L. Labrousse, L. Le Pourhiet, O. Lacombe, E. Lecomte, E. Burov, Y. Denèle, J.-P. Brun, M. Philippon, A. Paul, G. Salaün, H. Karabulut, C. Piromallo, P. Monié, F. Gueydan, A. I. Okay, R. Oberhänsli, A. Pourteau, R. Augier, L. Gadenne, and O. Driussi (2013), Aegean tectonics: Strain localisation, slab tearing and trench retreat, *Tectonophysics*, *597-598*, 1–33, https://doi.org/10.1016/j.tecto.2012.06.011.

Lallemand, S. E., P. Schnürle, and J. Malavieille (1994), Coulomb theory applied to accretionary and nonaccretionary wedges: Possible causes for tectonic erosion and/or frontal accretion, *Journal of Geophysical Research*, *99*(B6), 12,033–12,055, https://doi.org/10.1029/94jb00124.

Laurent, V., S. Scaillet, L. Jolivet, R. Augier, and V. Roche (2021), 40Ar behaviour and exhumation dynamics in a subduction channel from multi-scale 40Ar/39Ar systematics in phengite, *Geochimica et cosmochimica acta*, *311*, 141–173, https://doi.org/10.1016/j.gca.2021.06.001.

Lister, G. S., G. Banga, and A. Feenstra (1984), Metamorphic core complexes of Cordilleran type in the Cyclades, Aegean Sea, Greece, *Geology*, *12*(4), 221, https://doi.org/10.1130/0091-7613(1984)12<221:mccoct>2.0.co;2.

Lohrmann, J., N. Kukowski, C. M. Krawczyk, O. Oncken, C. Sick, M. Sobiesiak, and A. Rietbro (2006), Subduction channel evolution in brittle fore-arc wedges — a combined study with scaled sandbox experiments, seismological and reflection seismic data and geological field evidence, in *The Andes*, edited by O. Oncken, G. Chong, G. Franz, P. Giese, H.-J. Götze, V. A. Ramos, M. R. Strecker, and P. Wigger, pp. 237–262, Springer Berlin Heidelberg, https://doi.org/10.1007/978-3-540-48684-8_11.

Ludwig, K. R. (2008), Isoplot 3.70: geochronological toolkit for Microsoft Excel, *Berkeley Geochronology Center Special Publication*, *4*, 77.

Marsellos, A. E., W. S. F. Kidd, and J. I. Garver (2010), Extension and exhumation of the HP/LT rocks in the Hellenic forearc ridge, *American Journal of Science*, *310*(1), 1–36, https://doi.org/10.2475/01.2010.01.

Menant, A., L. Jolivet, and B. Vrielynck (2016a), Kinematic reconstructions and magmatic evolution illuminating crustal and mantle dynamics of the eastern Mediterranean region since the late Cretaceous, *Tectonophysics*, *675*, 103–140, https://doi.org/10.1016/j.tecto.2016.03.007.

Menant, A., P. Sternai, L. Jolivet, L. Guillou-Frottier, and T. Gerya (2016b), 3D numerical modeling of mantle flow, crustal dynamics and magma genesis associated with slab roll-back and tearing: The eastern Mediterranean case, *Earth and Planetary Science Letters*, *442*, 93–107, https://doi.org/10.1016/j.epsl.2016.03.002.

Menant, A., S. Angiboust, T. Gerya, R. Lacassin, M. Simoes, and R. Grandin (2020), Transient stripping of subducting slabs controls periodic forearc uplift, *Nature Communications*, *11*(1), 1823, https://doi.org/10.1038/s41467-020-15580-7.

Menant, A., R. Augier, E. Bessière, S. Angiboust, L. Jolivet, and O. Oncken (2026), Setting the Sequence of Slicing Events Along Deep Subduction Interfaces: 1. The Tectonic and Thermal Structure of the High-P Duplex in Western Crete (Hellenic Margin, *Tektonika*, *4*(1), 62–87, https://doi.org/10.55575/tektonika2026.4.1.106.

Meulenkamp, J. E., G. J. van der Zwaan, and W. A. van Wamel (1994), On late miocene to recent vertical motions in the Cretan segment of the Hellenic arc, *Tectonophysics*, *234*(1-2), 53–72, https://doi.org/10.1016/0040-1951(94)90204-6.

Mouslopoulou, V., G. M. Bocchini, S. Cesca, V. Saltogianni, J. Bedford, G. Petersen, M. Gianniou, and O. Oncken (2020), Earthquake swarms, slow slip and fault interactions at the western-end of the Hellenic Subduction System precede the M_w 6.9 Zakynthos Earthquake, Greece, *Geochemistry, Geophysics, Geosystems: G(3)*, *21*(12), https://doi.org/10.1029/2020gc009243.

Müller, W., R. D. Dallmeyer, F. Neubauer, and M. Thöni (1999), Deformation-induced resetting of Rb/Sr and ^{40}Ar/^{39}Ar mineral systems in a low-grade, polymetamorphic terrane (Eastern Alps, Austria), *Journal of the Geological Society*, *156*(2), 261–278, https://doi.org/10.1144/gsjgs.156.2.0261.

Nicol, A., V. Mouslopoulou, J. Begg, and O. Oncken (2020), Displacement accumulation and sampling of paleoearthquakes on active normal faults of Crete in the Eastern Mediterranean, *Geochemistry, Geophysics, Geosystems: G(3)*, *21*(11), https://doi.org/10.1029/2020gc009265.

Nocquet, J.-M. (2012), Present-day kinematics of the Mediterranean: A comprehensive overview of GPS results, *Tectonophysics*, *579*, 220–242, https://doi.org/10.1016/j.tecto.2012.03.037.

Noda, A. (2016), Forearc basins: Types, geometries, and relationships to subduction zone dynamics, *Geological Society of America Bulletin*, *128*(5-6), 879–895, https://doi.org/10.1130/b31345.1.

Papanikolaou, D. (1997), The tectonostratigraphic terranes of the Hellenides, *Ann. Geol. Pays Hellen.*, *37*, 495–514.

Papanikolaou, D., and E. Vassilakis (2010), Thrust faults and extensional detachment faults in Cretan tectono-stratigraphy: Implications for Middle Miocene extension, *Tectonophysics*, *488*(1-4), 233–247, https://doi.org/10.1016/j.tecto.2009.06.024.

Pourteau, A., R. Bousquet, O. Vidal, A. Plunder, E. Duesterhoeft, O. Candan, and R. Oberhänsli (2014), Multistage growth of Fe–Mg–carpholite and Fe–Mg–chloritoid, from field evidence to thermodynamic modelling, *Contributions to mineralogy and petrology. Beitrage zur Mineralogie und Petrologie*, *168*(6), 1090, https://doi.org/10.1007/s00410-014-1090-7.

Regard, V., J. Martinod, M. Saillard, S. Carretier, L. Leanni, G. Hérail, L. Audin, and K. Pedoja (2021), Late Miocene - Quaternary forearc uplift in southern Peru: new insights from 10Be dates and rocky coastal sequences, *Journal of South American Earth Sciences*, *109*(103261), 103,261, https://doi.org/10.1016/j.jsames.2021.103261.

Ring, U., and J. Glodny (2010), No need for lithospheric extension for exhuming (U)HP rocks by normal faulting, *Journal of the Geological Society*, *167*(2), 225–228, https://doi.org/10.1144/0016-76492009-134.

Ring, U., C. Fassoulas, I. T. Uysal, R. Bolhar, K. Tong, and A. Todd (2022), Nappe imbrication within the Phyllite-Quartzite Unit of west Crete: Implications for sustained high-pressure metamorphism in the hellenide subduction orogen, Greece, *Tectonics*, *41*(11), e2022TC007,430, https://doi.org/10.1029/2022tc007430.

Romer, T., S. Völs, B. Schulz, P. Xypolias, G. Zulauf, and E. Krenn (2008), Metamorphism of the pre-Alpine basement and the Phyllite-Quartzite Unit s.str. of Kythira (External Hellenides, Greece) [Metamorphose des präalpidischen Grundgebirges und der Phyllit-Quarzit-Serie i. e. S. Kythiras (Externe Helleniden, Griechenland.], *Zeitschrift der Deutschen Gesellschaft für Geowissenschaften*, *159*(3), 469–483, https://doi.org/10.1127/1860-1804/2008/0159-0469.

Scholl, D. W. (2021), Seismic imaging evidence that forearc underplating built the accretionary rock record of coastal North and South America, *Geological Magazine*, *158*(1), 104–117, https://doi.org/10.1017/s0016756819000955.

Seidel, E. (1978), Zur petrologie der Phyllit-Quartzit Serie Kretas, Ph.D. thesis, Braunschweig Univ., Braunschweig, Germany.

Seidel, E., H. Kreuzer, and W. Harre (1982), A late Oligocene/early Miocene high pressure belt in the external Hellenides, *Geol. Jahrb. , Reihe E*, *23*, 165–206.

Seidel, M., W. Zacher, W. H. Schwarz, P. Jaeckel, and T. Reischmann (2006), A Late Carboniferous age of the gneiss of Potamos (Kythira Island, Greece) and new considerations on geodynamic interpretations of the Western Hellenides, *Neues Jahrbuch für Geologie und Palaontologie. Abhandlungen*, *241*(3), 325–344, https://doi.org/10.1127/njgpa/241/2006/325.

Seidel, M., E. Seidel, and B. Stöckhert (2007), Tectono-sedimentary evolution of lower to middle Miocene half-graben basins related to an extensional detachment fault (western Crete, Greece), *Terra nova*, *19*(1), 39–47, https://doi.org/10.1111/j.1365-3121.2006.00707.x.

Shirzaei, M., R. Bürgmann, O. Oncken, T. R. Walter, P. Victor, and O. Ewiak (2012), Response of forearc crustal faults to the megathrust earthquake cycle: InSAR evidence from Mejillones Peninsula, Northern Chile, *Earth and Planetary Science Letters*, *333-334*, 157–164, https://doi.org/10.1016/j.epsl.2012.04.001.

Smye, A. J., L. V. Greenwood, and T. J. B. Holland (2010), Garnet–chloritoid–kyanite assemblages: eclogite facies indicators of subduction constraints in orogenic belts: GARNET-CHLORITOID-KYANITE ASSEMBLAGES, *Journal of Metamorphic Geology*, *28*(7), 753–768, https://doi.org/10.1111/j.1525-1314.2010.00889.x.

Smye, A. J., S. M. Seman, M. Scambelluri, P. G. Starr, and L. Federico (2021), Exhumation dynamics of high-pressure metamorphic rocks from the Voltri Unit, Western Alps: constraints from phengite Rb–Sr geochronology, *Contributions to mineralogy and petrology. Beitrage zur Mineralogie und Petrologie*, *176*(2), 14, https://doi.org/10.1007/s00410-020-01767-0.

Theye, T., and E. Seidel (1993), Uplift-related retrogression history of aragonite marbles in Western Crete (Greece), *Contributions to mineralogy and petrology. Beitrage zur Mineralogie und Petrologie*, *114*(3), 349–356, https://doi.org/10.1007/bf01046537.

Theye, T., E. Seidel, and O. Vidal (1992), Carpholite, sudoite, and chloritoid in low-grade high-pressure metapelites from Crete and the Peloponnese, Greece, *European Journal of Mineralogy*, *4*(3), 487–508, https://doi.org/10.1127/ejm/4/3/0487.

Thomson, S. N., B. Stöckhert, and M. R. Brix (1998), Thermochronology of the high-pressure metamorphic rocks of Crete, Greece: Implications for the speed of tectonic processes, *Geology*, *26*(3), 259, https://doi.org/10.1130/0091-7613(1998)026<0259:tothpm>2.3.co;2.

Tortorici, L., R. Caputo, and C. Monaco (2010), Late Neogene to Quaternary contractional structures in Crete (Greece), *Tectonophysics*, *483*(3-4), 203–213, https://doi.org/10.1016/j.tecto.2009.05.020.

Trotet, F., B. Goffe, O. Vidal, and L. Jolivet (2006), Evidence of retrograde Mg-carpholite in the Phyllite-Quartzite nappe of Peloponnese from thermobarometric modelisation - geodynamic implications, *Geodinamica acta*, *19*(5), 323–343, https://doi.org/10.3166/ga.19.323-343.

van Hinsbergen, D. J. J., and J. E. Meulenkamp (2006), Neogene supradetachment basin development on Crete (Greece) during exhumation of the South Aegean core complex, *Basin Research*, *18*(1), 103–124, https://doi.org/10.1111/j.1365-2117.2005.00282.x.

van Hinsbergen, D. J. J., and S. M. Schmid (2012), Map view restoration of Aegean–West Anatolian accretion and extension since the Eocene: RESTORATION OF THE AEGEAN REGION, *Tectonics*, *31*(5), https://doi.org/10.1029/2012tc003132.

van Hinsbergen, D. J. J., T. H. Torsvik, S. M. Schmid, L. C. Maţenco, M. Maffione, R. L. M. Vissers, D. Gürer, and W. Spakman (2020), Orogenic architecture of the Mediterranean region and kinematic reconstruction of its tectonic evolution since the Triassic, *Gondwana Research: International Geoscience Journal*, *81*, 79–229, https://doi.org/10.1016/j.gr.2019.07.009.

Vidal, O., B. Goffé, and T. Theye (1992), Experimental study of the stability of sudoite and magnesiocarpholite and calculation of a new petrogenetic grid for the system FeO–MgO–Al_2O_3–SiO_2–H_2O, *Journal of Metamorphic Geology*, *10*(5), 603–614, https://doi.org/10.1111/j.1525-1314.1992.tb00109.x.

Villa (1998), Isotopic closure, *Terra nova*, *10*(1), 42–47, https://doi.org/10.1046/j.1365-3121.1998.00156.x.

Villa, I. M., P. De Bièvre, N. E. Holden, and P. R. Renne (2015), IUPAC-IUGS recommendation on the half life of 87Rb, *Geochimica et cosmochimica acta*, *164*, 382–385, https://doi.org/10.1016/j.gca.2015.05.025.

Vitale Brovarone, A., and D. Herwartz (2013), Timing of HP metamorphism in the Schistes Lustrés of Alpine Corsica: New Lu–Hf garnet and lawsonite ages, *Lithos*, *172-173*, 175–191, https://doi.org/10.1016/j.lithos.2013.03.009.

von Huene, R., and D. W. Scholl (1991), Observations at convergent margins concerning sediment subduction, subduction erosion, and the growth of continental crust, *Reviews of Geophysics (Washington, D.C.: 1985)*, *29*(3), 279–316, https://doi.org/10.1029/91rg00969.

Wakabayashi, J. (2015), Anatomy of a subduction complex: architecture of the Franciscan Complex, California, at multiple length and time scales, *International Geology Review*, *57*(5-8), 669–746, https://doi.org/10.1080/00206814.2014.998728.

Walters, J. B. (2022), MinPlot: A mineral formula recalculation and plotting program for electron probe microanalysis, *Mineralogia*, *53*(1), 51–66, https://doi.org/10.2478/mipo-2022-0005.

Wang, K., L. Brown, Y. Hu, K. Yoshida, J. He, and T. Sun (2019), Stable forearc stressed by a weak megathrust: Mechanical and geodynamic implications of stress changes caused by the M = 9 Tohoku-Oki earthquake, *Journal of Geophysical Research. Solid Earth*, *124*(6), 6179–6194, https://doi.org/10.1029/2018jb017043.

White, R. W., N. E. Pomroy, and R. Powell (2005), An in situ metatexite–diatexite transition in upper amphibolite facies rocks from Broken Hill, Australia: IN SITU METATEXITE-DIATEXITE TRANSITION, *Journal of Metamorphic Geology*, *23*(7), 579–602, https://doi.org/10.1111/j.1525-1314.2005.00597.x.

White, R. W., R. Powell, T. J. B. Holland, T. E. Johnson, and E. C. R. Green (2014), New mineral activity–composition relations for thermodynamic calculations in metapelitic systems, *Journal of Metamorphic Geology*, *32*(3), 261–286, https://doi.org/10.1111/jmg.12071.

Whitney, D. L., and B. W. Evans (2010), Abbreviations for names of rock-forming minerals, *The American Mineralogist*, *95*(1), 185–187, https://doi.org/10.2138/am.2010.3371.

Wicker, V. (2023), Reconstructing the transition from the alpine subduction, late-orogenic extension and active rifting in the upper plate of a retreating orogenic system : A case study in the Aegean forearc, Southern Hellenides, Peloponnese, Greece. A field-based, structural, petrological and thermochronological approach, Ph.D. thesis, Université de Lorraine, Nancy, France.

Wicker, V., and S. Bufféral (2024), Deformation mechanisms during the syn-orogenic extrusion of the high-Pressure Phyllites-Quartzites unit in the central and northern Peloponnese, Greece, *Tectonics*, *43*(8), https://doi.org/10.1029/2023tc008116.

Xypolias, P., and I. K. Koukouvelas (2001), Kinematic vorticity and strain rate patterns associated with ductile extrusion in the Chelmos Shear Zone (External Hellenides, Greece), *Tectonophysics*, *338*(1), 59–77, https://doi.org/10.1016/s0040-1951(01)00125-1.

Zachariasse, W. J., and D. van Hinsbergen (2025), Is there a Cretan supradetachment basin? Insights from detailed mapping on northwestern Crete (Greece), *Tektonika*, *3*(2), https://doi.org/10.55575/tektonika2025.3.2.97.

Zachariasse, W. J., D. J. J. van Hinsbergen, and A. R. Fortuin (2011), Formation and fragmentation of a late Miocene supradetachment basin in central Crete: implications for exhumation mechanisms of high-pressure rocks in the Aegean forearc: Formation and fragmentation of a late Miocene supradetachment basin, *Basin Research*, *23*(6), 678–701, https://doi.org/10.1111/j.1365-2117.2011.00507.x.

Zulauf, G., W. Dörr, L. Marko, and J. Krahl (2018), The late Eo-Cimmerian evolution of the external Hellenides: constraints from microfabrics and U–Pb detrital zircon ages of Upper Triassic (meta)sediments (Crete, Greece), *International Journal of Earth Sciences*, *107*(8), 2859–2894, https://doi.org/10.1007/s00531-018-1632-8.